

Bachelor Thesis

cand. mach. Juan Calejero Martínez

Matrikelnr.: 2077945

**Research about geometrical errors produced in Computed
Tomography machine for
dimensional metrology**

wbk

Institute of Production Science
Karlsruhe Institute of Technology (KIT)
Kaiserstraße 12
76131 Karlsruhe

Prof. Dr.-Ing. Jürgen Fleischer
Prof. Dr.-Ing. Gisela Lanza
Prof. Dr.-Ing. habil. Volker Schulze

Statement of Originality

I sincerely affirm to have composed this thesis work autonomously, to have indicated completely and accurately all aids and sources used and to have marked anything taken from other works, with or without changes. Furthermore, I affirm to have observed the constitution of the KIT for the safeguarding of good scientific practice, as amended.

Karlsruhe, March 31st 2017

Juan Calejero Martínez

Acknowledgement

I would like to extend my sincere gratitude to my supervisors Alexandra Krämer from Karlsruhe Institute for Technology and Jose Antonio Yagüe Fabra from Universidad de Zaragoza, my colleague from WBK Timm Schneider, the workshop team from WBK and to Waterworxx GmbH.

Abstract

Computed Tomography, also known as CT, is a new method in dimensional metrology. As conventional procedures cannot reach internal features of the measured object, like tactile CMMs, CT enables an entire measurement of the workpiece including the intern geometry. It is a non-destructive method with much potential to be developed (Thompson A., Maskery I., Leach R. 2016). However, CT is influenced by numerous sources of error which may have negative impact on the accuracy and repeatability of dimensional and geometrical measurements.

This thesis is focused on the geometrical error estimation produced by the sources of error, like focal spot movement and angular misalignments of the detector.

In order to determine the effect of those sources of error mentioned previously, it necessary to compare the measurands of the CT with the measurands done by a higher precision method like Coordinate Measuring Machine (CMM).

The object of this comparison was the reference object CT Ball Plate.

This reference object was imaged at different magnification distances in the CT and then those scans done in CT were processed in MatLab to detect the projections of the spheres, including their centres and radii. Therefore, the distances between sphere centres measured by CT were known.

Those measurands from the CT were compared to the measurands of the CMM, so as to see the scale error produced in the CT process. Then, that error was related lineally in Excel with the actual CMM distance, taken as a reference value. As a result, a mathematical relation between the error of the CT and the object measurands was obtained.

Additionally, as the detector could be tilted, slanted or skewed, a method to calculate those angular misalignments via trigonometrical procedures was given and applied to obtain those deviations. As a result, tilt and slant were around $1,64^{\circ}$ and skew around $0,26^{\circ}$.

Table of Contents

Table of Abbreviations	IV
1 Introduction	1
1.1 Motivation	1
1.2 Objective	2
2 Background	3
2.1 Computed Tomography machine	3
2.1.1 The source. Physical principles: X-Ray production	3
2.1.2 Interaction of X-Rays with matter	6
2.1.3 The X-Ray detector	8
2.1.4 Kinematic systems	9
2.1.5 Software	10
2.1.6 Advantages and disadvantages of CT	11
2.1.7 Different types of CT	11
2.2 Potential sources of error	12
2.2.1 Beam hardening	13
2.2.2 Scattering	14
2.2.3 Temperature	14
2.2.4 Performance, scanning methods and measurement strategy	15
2.2.5 User influence	15
2.2.6 Threshold and noise	15
2.3 Sources of geometrical error	16
2.3.1 Angular misalignments of the detector	17
2.3.2 Focal spot movement	19
2.4 Measurement uncertainty in CMMs	21
3 State of the art	24
3.1 Previous methods	24
3.2 Reference objects	31
4 Own approach	35
4.1 Development of CT Ball Plate	35
4.2 CT Ball Plate calibration in CMM	37
4.3 Explanation of the experiments in CT	40
4.3.1 Estimation of angular misalignments of the detector	52

4.3.2 Estimation of scale error	59
5 Results	61
5.1 Results from estimation of angular misalignments of the detector	61
5.2 Results from estimation of scale error	62
6 Discussion	64
7 Summary and Outlook	65
8.1 Summary	65
8.2 Outlook	65
List of Figures	66
List of Tables	69
References	70
Appendix	74

Chapter 1 contains a brief introduction about the recently new technology of CT and the motivation that was behind the thesis itself.

Chapter 2 gives an explanation of all the background behind the thesis, which is completely necessary to understand the thesis and the results obtained from it, in terms of components, physical principles, sources of deviation, geometrical error in CT and additionally a section about measurement uncertainty in CMM.

Chapter 3 contains the state of the art, all those studies that made possible the development of the methods used in this thesis to estimate the geometrical error produced in CT, also there is a section about reference objects, as the reference object used in this thesis is based on another object developed previously by DTU.

Chapter 4 fully explains the own approach developed in this thesis, in terms of the methods to estimate geometrical sources of error, tools, programs and procedures to use both machines, CMM and CT.

Chapter 5 contains the results of the methods exposed in Chapter 4.

Chapter 6 contains an explanation of the results from Chapter 5, in terms of validity, whether is a proper estimation or not and accurateness of results. Also, it contains the steps that should be followed to improve the accurateness of the method.

Chapter 7 contains a summary of all the work done and the outlook derived from it.

1 Introduction

1.1 Motivation

“Measure what can be measured, and make measurable what cannot be measured.”

This very popular quotation (Galileo Galilei 1602), fits perfectly with the scenario of the Computed tomography (CT) technology in metrology applications. As it is a recent technology, it needs further investigation to quantify the errors produced in a CT scan in order to enhance the accurateness of the method (Massimiliano Ferrucci, Richard K Leach, Claudiu Giusca, Simone Carmignato and Wim Dewulf 2015).

Computed tomography (CT) is a technique that uses the attenuating properties of a medium as X-rays propagate through it. The image obtained is then projected in a detector behind the object. In this detector, all information is gathered and computed by a reconstruction software which gives a 3D model where the measurement can be made.

Since its discovery, CT has been used in the medical field as a method to inspect inside the human body. Afterwards, the technology was applied on the industrial inspection of manufactured parts, the valuable fact of this technique for manufacturers was the possibility to examine the material structure and inner defects of their product in a way that would be dangerous for the product's physical integrity. More recently, CT has been recognized as a powerful method for metrology of assembled and complex parts, (Thompson A., Maskery I., Leach R. 2016).

CT stands out, because it provides the user with the ability to perform dimensional analysis on internal features that are unreachable by conventional coordinate measuring machines (CMMs), it is faster than a CMM complete analysis and it offers a complete 3D model of the scanned object in a computer (Muller P 2012), (De Chiffre L., Carmignato S., Kruth J. P., Schmitt R., Weckenmann A. 2014), (Kruth J.P., Bartscher M., Carmignato S., Schmitt R., De Chiffre L., Weckenmann A. 2011), (Weckenmann A., Krämer P. 2010).

1.2 Objective

CT technology has much potential to be developed and several features that make this technology to stand out among traditional techniques.

However, several problems are accompanied with this procedure. It is generally accepted that sources of error like: beam hardening, scattering, focal spot movement, angular misalignments of the detector, noise and reconstruction software errors will cause deviations in measurands (Muller P 2012).

Among all these potential sources of error, this thesis will be focused on those sources that create geometrical error: focal spot movement and angular misalignments of the detector.

The focal spot movement is a consequence of the X-Rays production, as it is originated due to the vibration of the X-Ray source when it is heated. This focal spot movement complicates the acquisition of an accurate image.

The angular misalignment of the detector is caused by the rotation of the detector in some axis (tilt, slant and skew) which creates a deformed image.

A comparison method will be used to obtain the estimation of the scale error.

First, the reference object, called CT Ball Plate previously developed by DTU (Muller P 2012), will be measured using a tactile CMM, those measurands will be taken as reference values.

Second the CT machine will be used to measure the CT Ball Plate.

By comparing those measurands obtained from CT and CMM, it will be possible to obtain a mathematical relation between the geometrical error produced by CT and the real measurand of the object.

Additionally, by using those measurands from the CT, the misalignment angles from the detector (tilt, slant and skew) can be estimated by trigonometrical relations.

The quantification of that geometrical error will be the main purpose of the thesis.

2 Background

2.1 Computed Tomography machine

2.1.1 The source. Physical principles: X-Ray production

The X-ray source is made of several components: an electron beam gun which includes a cathode filament that emits electrons, an anode accelerating those electrons, a Wehnelt grid electrode for controlling the electron beam, in terms of convergence and intensity of beam, and some magnetic deflectors and lenses to focus the electron beam in a target that will produce X-rays, see Figure 2-1.

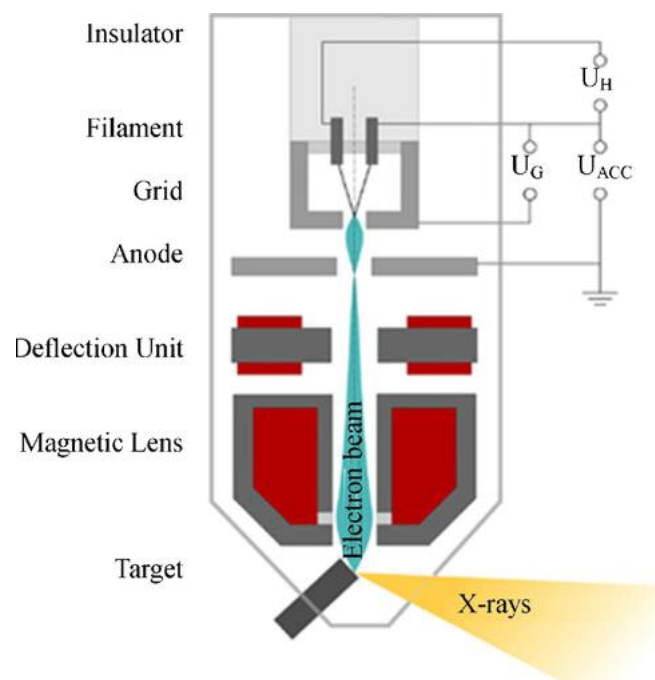


Figure 2-1: Typical X-ray source. (J.P. Kruth, M. Bartscher, S. Carmignato, R. Schmitt, L. De Chiffre, A. Weckenmann 2011).

As electrons hit the target, the fast electrons are decelerated, leading to the conversion of their energy into: heat (over 99%) and X-rays (around 1%).

It is crucial to have a small electron beam or X-ray spot in order to obtain sharp images. The reduction of the diameter of the spot is feasible by augmenting the photon energy, (this energy is measured in keV, defined as the energy of an electron when accelerated by an applied voltage in kV), but there is an upper limit for this energy, because for very high voltages, the heat dissipated at the target gets so big that it may no longer be focused in a concrete precise spot due to vibration. Today commercial standard X-ray sources have a voltage limit around 450 kV (J.P. Kruth, M. Bartscher, S. Carmignato, R. Schmitt, L. De Chiffre, A. Weckenmann 2011).

At the exit of the X-ray source, the X-ray beam is shaped by passing through a circular hole or diaphragm, for conical beams.

The target of the source can be made from different materials, giving different X-ray radiation spectra respectively. It can be a transmitting target (thin plate) or a reflective target (massive target). Thin transmitting targets are found in low power CT sources, as they cannot withstand

high temperatures. Whereas, high power CT sources usually use water cooled massive reflective targets in order to withstand the high temperatures. Some sources have multi-material targets, used for example when measuring multi-material objects and lower absorbing objects, which contain materials like plastics and foams.

The produced X-ray radiation consists of “Bremsstrahlung radiation” and “characteristic radiation”, see Figure 2-2.

Bremsstrahlung is the dominant X-ray production process. It takes place when an electron hits an atomic nucleus in the target, resulting in a deceleration of the electron and in an emission of an X-ray photon. Bremsstrahlung gives a constant X-ray spectrum from very low energies up to the energy of the impacting electron.

Characteristic radiation exists when a high-energy electron impacts and excites an inner shell electron in an atom of the target. De-excitation of this high-energy electron or the fact that it becomes a replacing electron (in case that the inner shell electron is ejected and the void is filled) produces a delivery of energy from electron and a photon of characteristic radiation. Its name “characteristic” comes from the fact that radiation energy depends on the target material and is characterized by a line spectrum.

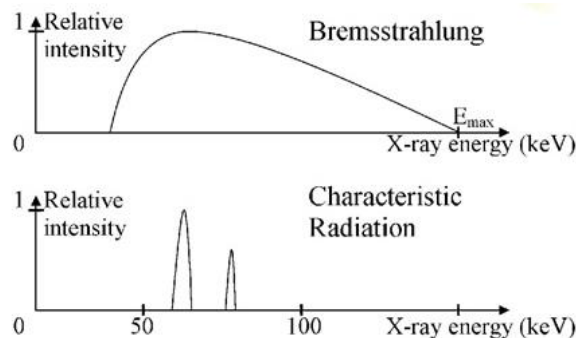


Figure 2-2: Radiation spectra. (J.P. Kruth, M. Bartscher, S. Carmignato, R. Schmitt, L. De Chiffre, A. Weckenmann 2011).

The originated X-ray radiation is characterized by: energy distribution, also known as quality, and intensity, also known as flux. The highest X-ray energy from the X-ray spectrum limits the penetrating power of the X-ray beam into matter. The intensity of X-ray beam is a quantification of the amount of radiation energy flowing per unit of time.

2.1.1.1 X-ray source current and voltage

The power of an X-ray beam is characterized by that voltage and that current applied on the electron beam which reaches the target and generates X-rays.

The current, in μA , quantifies the rate of charge carriers or electrons, flowing from the filament of the source to the target. It influences the X-ray intensity (quantity or amount of radiation energy), but has no effect on the beam quality or penetration power.

As appears in Figure 2-3 making double the current doubles the intensity across all photon energies of the spectrum, (Bartscher M, Neuschaefer-Rube U, Wäldele F 2004).

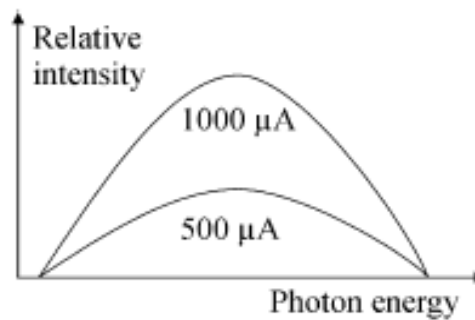


Figure 2-3: Influence of source current. (J.P. Kruth, M. Bartscher, S. Carmignato, R. Schmitt, L. De Chiffre, A. Weckenmann 2011).

The voltage (kV) has effect on both, quality and intensity. It affects quality due to the fact that the voltage determines the maximum photon energy and hence the penetration power. In Figure 2-4 the effects of doubling the voltage are presented.

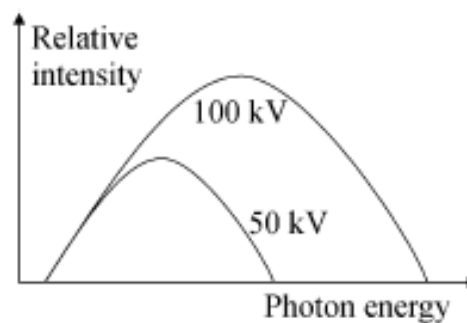


Figure 2-4: Influence of source voltage. (J.P. Kruth, M. Bartscher, S. Carmignato, R. Schmitt, L. De Chiffre, A. Weckenmann 2011).

Voltage and current selection for a specific measurement is not an easy task. The voltage changes hugely the X-ray spectrum as includes new specific radiation peaks in the spectrum. It leads to a dilemma: the voltage should on the one hand be high enough to avoid total beam extinction in the direction where the largest quantity of material has to be penetrated, but may on the other hand not lead to a loss of contrast or saturation of the detector in the direction where less material is gathered. This situation might present a problem when measuring pieces that are thick in one direction and thin in other directions or when measuring parts made of different materials.

2.1.1.2 Filtration

Filtration is a common way to reduce the effect of beam hardening, which will be introduced later on in section 2.2.1. These filters are made of different materials, for example: aluminium, copper, brass; and are used to harden the X-ray spectrum generated by the X-ray source, in other words filters are used to provide a cleaner image. By using such filters low energy photons are filtered out. The emission spectrum is not modified but increases the average energy of the X-ray beam with an increase of quality and a reduction of quantity, in terms of total energy, see Figure 2-5. The amplitude gets smaller and the spectrum is moved rightwards, that means higher energy levels. However, this method includes one disadvantage: when the low energy photons are filtered out, the number of X-rays is decreased resulting in decrease of the image signal-to-noise ratio (SNR).

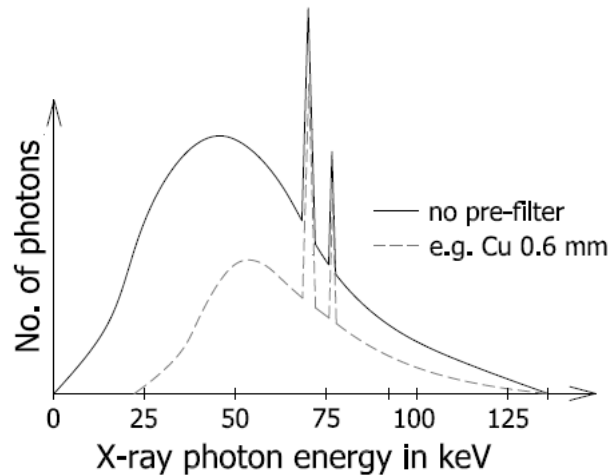


Figure 2-5: Factors affecting size and relative position of X-ray spectrum. (Muller P 2012)

2.1.1.3 Target material

In terms of selecting the right target material, X-rays with higher energy penetrate more effectively than lower energy ones. Then materials with high atomic number, like tungsten or gold enable to reach higher penetration, augmenting the efficiency of X-ray generation, in terms of quantity and quality of X-rays, see Figure 2-6.

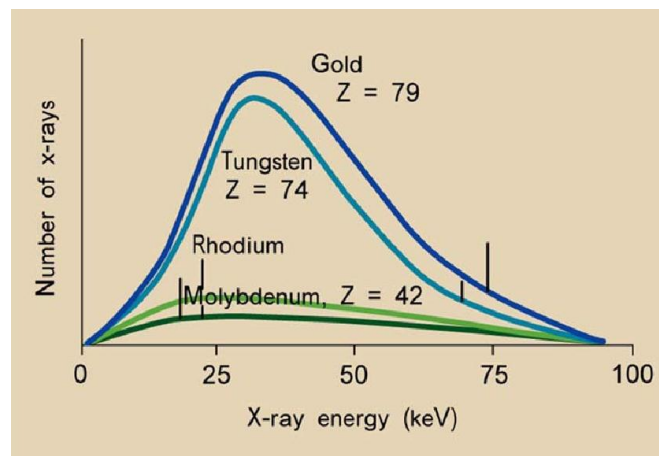


Figure 2-6. (Pavel Müller 2011)

2.1.2 Interaction of X-rays with matter

When the X-Rays interact with the object, the intensity of the rays decreases due to absorption and scattering. The contributions for the attenuation are photoelectric effect and Compton (scatter) effect. Both depend on the energy.

The intensity loss is described by Lambert-Beer's law, equation 2-1. The law says that each layer of equal thickness gets an equal part of the radiation that traverses it. This can be expressed as follows:

$$\frac{dI}{I} = -\mu ds$$

Equation 2-1

The parameters express: I is intensity of the incident radiation, dI/I is fraction of radiation removed from the beam as it traverses a small thickness ds of material and μ is linear attenuation coefficient. After integrating equation 2-1, this equation is obtained:

$$I = I_0 e^{-\mu ds} \quad \text{Equation 2-2}$$

where I_0 and I are X-ray intensities, initial (unattenuated) and final (transmitted through the material of thickness s). When X-rays travel through an inhomogeneous material, equation 2-2 must be rewritten:

$$I = I_0 e^{-\int \mu ds} \quad \text{Equation 2-3}$$

The line integral is taken along the propagation direction and $\mu(s)$ is the linear attenuation coefficient at each point on the ray way. The linear attenuation coefficient is a measure of the attenuation per unit distance. It is specific for the used X-ray energy and for the type of absorber. Consequently, equation 2-3 should be adapted for inhomogeneous materials and polychromatic X-Rays:

$$I = I_0(E) e^{-\int \mu(s,E) ds} dE \quad \text{Equation 2-4}$$

The linear attenuation coefficient represents the number of atoms in a cubic cm volume of material and the chance of a photon being absorbed or scattered from a nucleus or an electron of one of these atoms. The number of photons transmitted through a material is affected by the thickness, density and atomic number of the material and the energy of the individual photons, and generally reduces exponentially while travelling through the matter which can be seen in Figure 2-7.

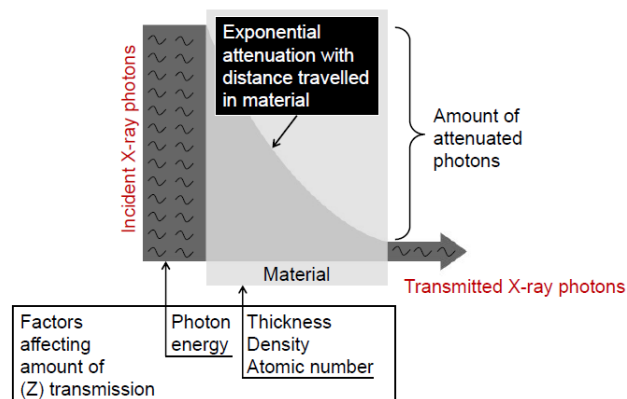


Figure 2-7: Emitted and transmitted photons dependence. (Muller P 2012)

In theory, the interaction of the X-rays with matter can result in three different scenarios: the incident X-ray can be completely absorbed; the incident X-ray can scatter elastically; or the incident X-ray can scatter inelastically.

The most important photon-matter interactions for radiography are: photoelectric effect, Compton scattering, or incoherent scattering, and pair production. Other possible interaction is Rayleigh scattering, or coherent scattering, which is small but non-negligible. So then, the linear attenuation coefficient can be written as:

$$\mu = \mu_{ph} + \mu_{incoh} + \mu_{coh} + \mu_{pp}$$

Equation 2-5

However, only the photoelectric absorption and the Compton effect are important in the energy ranges used in X-ray CT. This will be further explained in section 2.2.2 Scattering.

2.1.3 The X-Ray detector

The CT detector is where all the information from the scan is gathered, nowadays there are two types of CT detectors: flat panel detectors consisting of a 2D array of pixels and straight or curved line detectors consisting of a 1D array of pixels. The difference is presented in Figure 2-8.

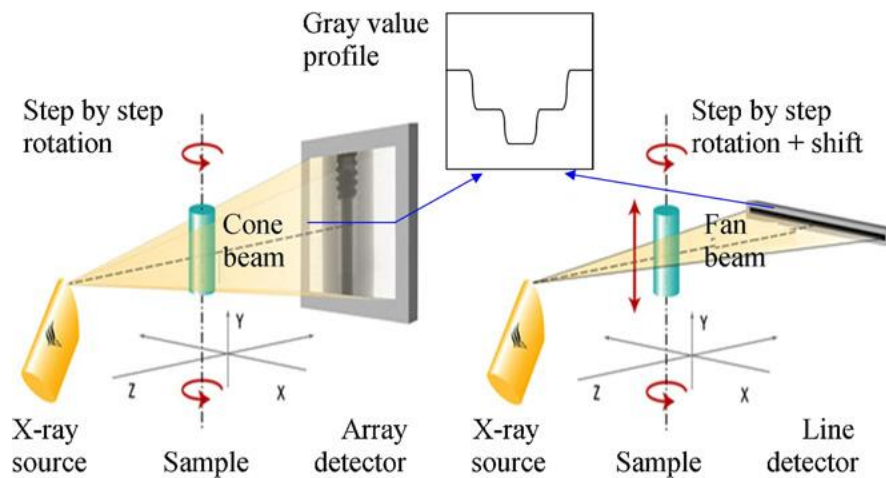


Figure 2-8: 2D flat panel detector with cone beam and 1D line detector with fan beam. A grey value profile along one pixel line is shown. (J.P. Kruth, M. Bartscher, S. Carmignato, R. Schmitt, L. De Chiffre, A. Weckenmann 2011).

1D line detectors offer a higher accuracy, higher efficiency and withstand higher X-ray energies suitable when measuring thicker objects. Nevertheless, a complete object scan with line detector takes more time as only one slice is measured per rotation of the workpiece and as the object should be moved vertically to get more slices.

The higher accuracy is because line detectors use collimated X-ray beams, fan beam rather than cone beam, and get then less pixel interaction or scatter.

Basically, there are three detector factors. The information of the detector is in proportion with: the total number of photon impacts (counting-type detectors), in proportion with the total photon energy (scintillation-type detectors or indirect detectors), or in relation with the energy deposition per unit mass (ionization detectors), (Kak AC, Slaney M 1988). The most commonly used detectors are indirect, (Bartscher M, Neuschaefer-Rube U, Wäldele F 2004).

The common commercial 2D detectors have a maximum resolution of 2048x2048 pixels at a pixel size of 200 μm and withstand up to about 250 keV. At high power (80 keV to 10 MeV), 1D detectors are used, which may include over 3000 pixels at pixel size of 250 μm .

2.1.4 Kinematic systems

Normally in CT scans, X-ray source and detector are fixed, while the object rotates somewhere between source and detector. It could be without translation movement, when using a 2D detector, or with a vertical translation, when using a 1D detector. The basic axes configuration of industrial CT scanners is given in Figure 2-8.

The common kinematic system is composed of:

- A turntable for stepwise or continuous rotation of the workpiece.
- A horizontal translation axis for positioning the turntable with the workpiece somewhere between the X-ray source and the detector, in image 2.8 it is presented as Z-axis. This axis is usually named as the magnification axis: higher magnification is achieved by positioning the object closer to the source, see Figure 2-9. When magnification augments, it increases the image resolution, but it also creates more blurred images, due to the finite X-ray spot size.
- Sometimes there is a horizontal translation axis in X-direction to move the turntable parallel to the detector. This translation axis allows placing the workpiece in and outside the field of measurement.
- A vertical translation axis moving turntable. When using 2D flat panels is not so indispensable, this axis is used for placing the workpiece in the detector. When using 1D detectors, the vertical axis is completely necessary.

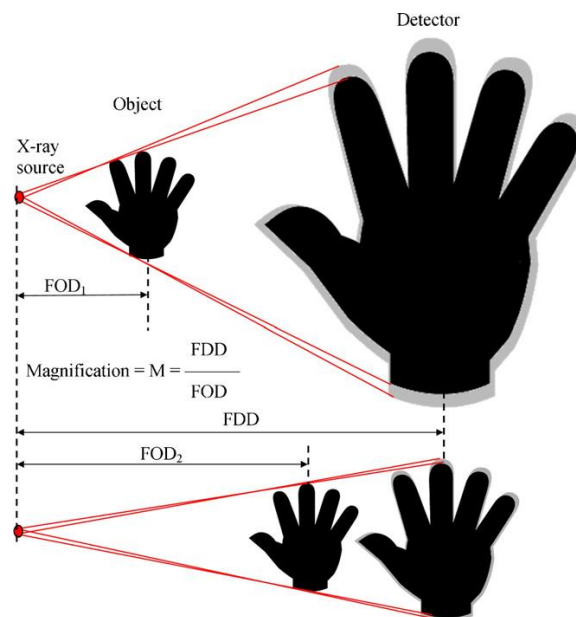


Figure 2-9: Image magnification and blurring. (J.P. Kruth, M. Bartscher, S. Carmignato, R. Schmitt, L. De Chiffre, A. Weckenmann 2011).

It is extremely recommended a high accuracy and stability (geometrical and thermal) as they affect measurement results: positioning errors of the rotating platform and its rotation quality affect the quality of reconstruction; positioning errors and repeatability of the Z-axis is directly related with the measured dimensions through a change in magnification factor.

2.1.5 Software

Apart from importance of the CT hardware, software is of extreme importance, more specifically for the reconstruction of the volume model when acquired 2D projection images. Reconstruction is usually carried out by filtered back-projection, which is based on the Linear Integral Transformation. As mentioned in section 2.1.2, the model describes the absorption of X-rays when passing through a medium with varying linear attenuation coefficient μ , remembering Equation 2-3:

$$I = I_0 e^{-\int \mu ds} \quad \text{Equation 2-3}$$

which goes back to the Beer–Lambert law which expresses the exponential attenuation of electromagnetic radiation with initial intensity I_0 traveling a distance s in an absorbing medium μ , remembering Equation 2-2:

$$I = I_0 e^{-\mu ds} \quad \text{Equation 2-2}$$

The data for the reconstruction are the grey value profiles, remember Figure 2-8, representing the intensity along the pixels on one line of the detector.

When using cone beam, the reconstruction need to take into account that voxels do not remain in the same horizontal projection plane as the part rotates. The reconstruction is then based on the Feldkamp algorithm.

As appears in Figure 2-10, the result of the reconstruction increases in quality when increases the number of angular poses, in this case from 4 to 128. With 4 angular poses the reconstruction is very bad. As the number of poses augments, the reconstruction becomes more precise, ending with an accurate picture of the three spheres.

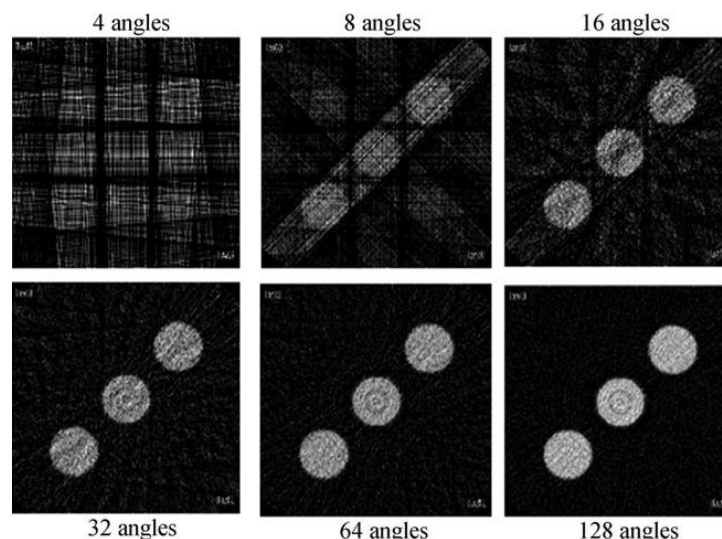


Figure 2-10: More angular poses improve reconstruction accuracy, but enlarge measurement time. (J.P. Kruth, M. Bartscher, S. Carmignato, R. Schmitt, L. De Chiffre, A. Weckenmann 2011).

As a result of all these, it is easy to notice that the quality of reconstruction is influenced by: pixels size; number of pixels within each grey value profile, that means number of detector pixels in X-direction; number of detector pixels or slices in the Y-direction, which is not necessarily the same as the number of pixels in the Y-direction for a flat panel detector; number of angular positions, or poses, at which images are taken and number of projection images taken at each angular pose.

The 3D reconstruction process is followed by the edge or surface detection or segmentation which differences between solid materials and surrounding air or between different solid materials, it will be introduced later on in section 2.2.6.

2.1.6 Advantages and disadvantages of CT

Advantages (Muller P 2012), (De Chiffre L., Carmignato S., Kruth J. P., Schmitt R., Weckenmann A. 2014), (Kruth J.P., Bartscher M., Carmignato S., Schmitt R., De Chiffre L., Weckenmann A. 2011), (Weckenmann A., Krämer P. 2010):

- Non-destructive
- Short scanning time
- Volume data of high density
- Determination of inner and outer geometry

Disadvantages (Muller P 2012), (De Chiffre L., Carmignato S., Kruth J. P., Schmitt R., Weckenmann A. 2014), (Kruth J.P., Bartscher M., Carmignato S., Schmitt R., De Chiffre L., Weckenmann A. 2011), (Weckenmann A., Krämer P. 2010):

- Complex and numerous influence quantities affecting measurements
- Reduced measurement capability due to measurement errors
- Problem encountered when scanning multi-material objects
- Measurement uncertainty in many cases unknown (results are not traceable)

2.1.7 Different types of CT

There are various types of CT systems available nowadays, from small devices which can be attached inside a Scanning Electron Microscope (SEM) to large machines used for CT scanning of big parts (L. De Chiffre, S. Carmignato, J.-P. Kruth, R. Schmitt, A. Weckenmann 2014).

These are the main types of CT machine:

- Clinical CT: in clinical CT scanners, the X-ray unit, including source and detector, is continuously rotating around the object or patient, which lays stationary or is slowly moved horizontally to obtain tomographic images representing slices of the scanned body.
- Material analysis and industrial CT: the object is rotated in the X-ray beam, while X-ray source and the detector remain stationary. As the object is closer to the source, higher image magnification and higher pixel resolution are obtained however blurring augments. When the object is closer to the detector, sharper images and less resolution are achieved.
- Dimensional metrology CT
- Robot operated CT: loading and unloading of the scanning objects can be automatized.
- SEM CT

- Large scale CT
- Linear accelerators and synchrotron CT: present another possibility to accelerate electrons against a target. Linear accelerators augment the speed of electrons, or other charged particles, by exposing them to oscillating electric potentials. Due to its high energy, linear accelerators can be used for penetrating very thick and/or high absorbing parts like concrete or metal.

2.2 Potential sources of error

When it comes to CT, there is a wide variety of influencing factors, see Figure 2-11 from DTU (Pavel Müller 2011). Those influence factors divided into five different groups: factors connected with the hardware (X-ray source, rotary table, X-ray detector and performance), software/data processing (3D reconstruction, threshold determination and surface generation, data corrections and data reduction), environment (temperature, vibrations, humidity), measurement object (penetration depth, geometry and dimension, beam hardening, scattered radiation, material, roughness) and operator (scanning parameters).

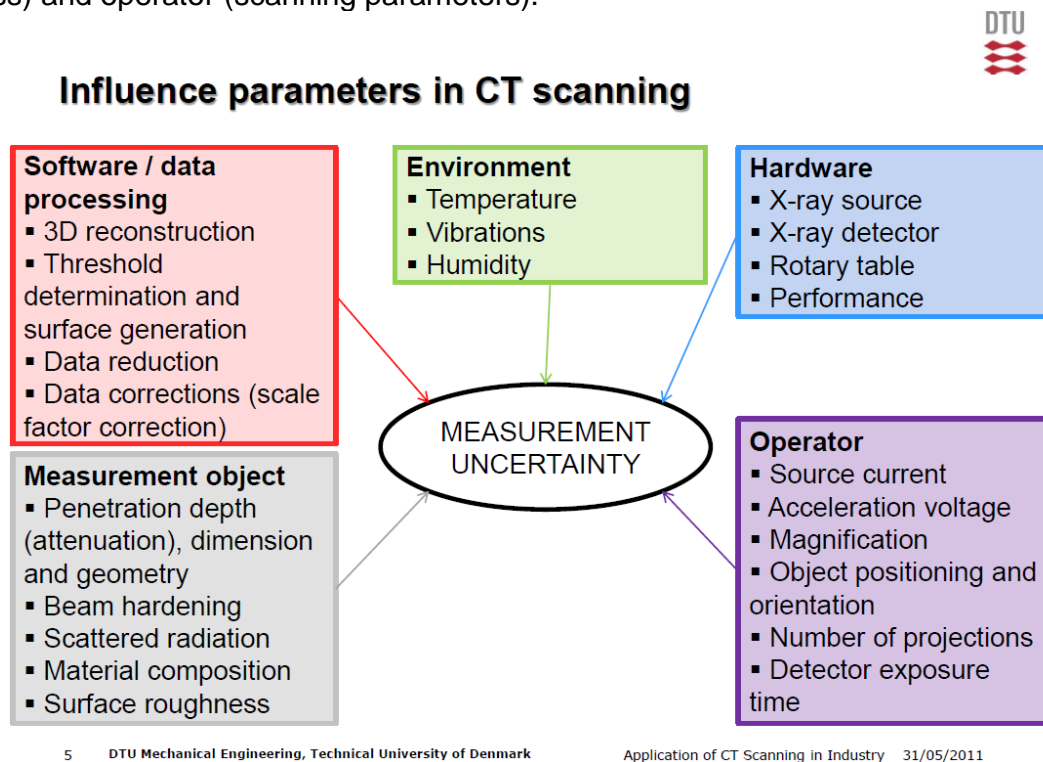


Figure 2-11: Scheme of CT influence factors from DTU. (Pavel Müller 2011)

All these influence factors mixed produce errors in the final measurement and it is difficult to isolate the effect of one source of error from the rest in the final result.

2.2.1 Beam hardening

When X-ray beams traverse matter there is a spectrum of different energies. Polychromatic X-ray beams with the lowest energies are absorbed firstly. Thus, only X-rays with higher energies remain in the beam when going through matter, as these high-energy X-rays are less likely to be

attenuated. Also, the longer the X-ray paths through the object are, the more low-energy-photons are absorbed, giving a more penetrating beam (because the mean energy is augmented). It could be said that the beam becomes “harder” therefore is called beam hardening. Then, for polychromatic radiation, the total attenuation is not a linear function of object’s thickness. This non-linear beam hardening effect needs to be equilibrated, otherwise the reconstructed images in X-ray CT will be deviated by artifacts, for example edge artifacts, streaks, etc. Beam hardening makes it more difficult to understand the measured data quantitatively because it changes the attenuation. This complicates the threshold determination and resolution. As a result, higher measurement errors are expected if no beam hardening correction is applied. Correcting the beam hardening effect plays a vital role in CT (M. Franz, Ch. Funk, J. Hiller, S. Kasperl, M. Krumm, S. Schröpfer 2009), (R. A. Ketcham, W. D. Carlson 2001), (T. Paul, Z. He 2008), (S. Kasperl, J. Hiller, M. Krumm 2009). A reduction of beam hardening effect can be done by pre-hardening of the beam using physical filters (aluminium, copper, brass, etc.) as commented in section 2.1.1.2. Also, monochromatic radiation is an effective method, (U. Bonse, F. Busch 1996), (O. Brunke, K. Brockdorf, S. Drews, B. Müller, T. Donath, J. Herzen, F. Beckmann 2008). This radiation could be provided by a synchrotron, see section 2.1.7. The characteristic curves for monochromatic and polychromatic radiation are presented in Figure 2-12.

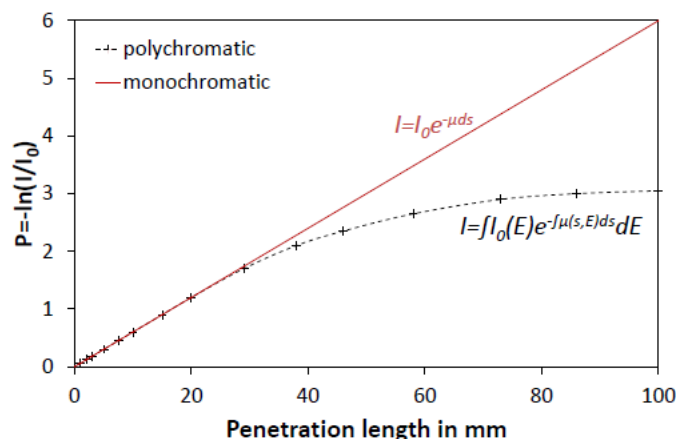


Figure 2-12: Mono- and polychromatic radiation curves. (Muller P 2012)

It is clearly seen that the intensity change is linear for monochromatic radiation and non-linear for polychromatic radiation.

Linearization process is another typical method, it can be done with two techniques:

- Based on a reference object (G. T. Herman 1979), (G. T. Herman, 1980), (R. A. Brooks, G. Di Chiro 1986): the relation between the propagated path length and the weakened intensity is estimated. The characteristic line is then used to compute beam hardening corrected intensity values allowing the reconstruction of an artifact-free CT image. This can be obtained by using a step wedge (S. Kasperl, J. Hiller 2009), it needs to have the same material as the specimen.
- Software based: known as Iterative Artifact Reduction (IAR) method, is an iterative process in which several post-processing steps are applied to the reconstructed volume to compute a beam hardening correction without reference objects. The IAR method requires projection information and is valid only for homogeneous objects. This method was developed at (S. Kasperl, J. Hiller, M. Krumm 2009).

2.2.2 Scattering

Scattering is caused by deflection of X-rays inside the material of the measured object or the detector. Often, scatter produces a halo surrounding the object and reduces the signal-to-noise (S/N ratio). The effects of scatter and/or beam hardening can be reduced by algorithms, for example effect on attenuation. Those effects can also be minimized by thresholding.

There are two types of scattering distinguishable: coherent scattering and incoherent scattering as commented in section 2.1.2. Incoherent scattering has a bigger effect on the total attenuation for photon energies bigger than 120keV, (Jochen Hiller, Peter Hornberger 1996), see Figure 2-13. It is expected to have signal and noise contributions in the CT image from scattered photons due to coherent (Rayleigh) and incoherent (Compton) scattering.

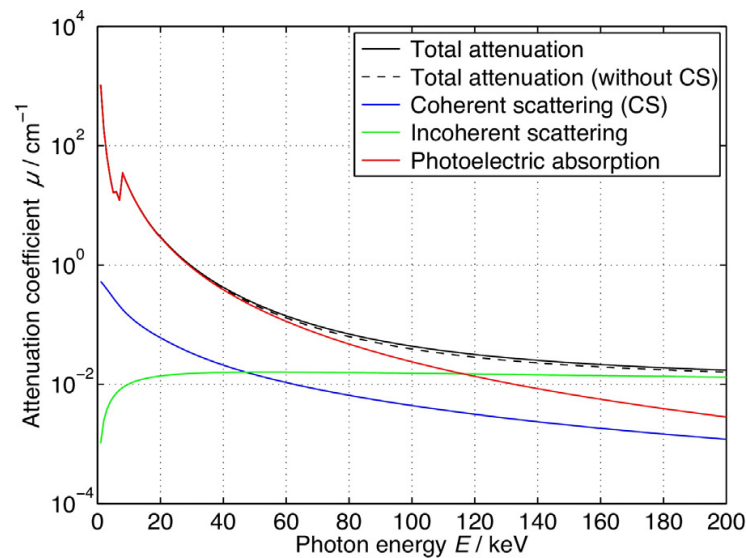


Figure 2-13: Energy-dependent linear attenuation coefficients. (Jochen Hiller, Peter Hornberger, 1996)

2.2.3 Temperature

As opposed to medical or material inspection applications, dimensional metrology applications in CT require measurements to be at 20 °C and deviation from this standard temperature produces errors.

Temperature control in dimensional CT is not easy as in other procedures, due to the fact that CT contains a heat source inside the machine itself, the X-ray source. Additionally, motors, drives, detector and electronics might be considered as heat sources.

Traceable measurements are only possible if all elements; taking into account detector, structure separating source/workpiece/detector, workpiece itself; are at uniform and stable temperature, around $20 \pm 0.1-0.5$ °C.

If thermal error correction is applied, it needs to take into account, not only deviations from the standardized 20 °C, but also thermal gradients and transients that may occur around this temperature. It is necessary to have a thermally stabilized CT machine.

2.2.4 Performance, scanning methods and measurement strategy

The way to do the measurement of a piece with the CT could also be taken as an influence factor. Nowadays, two main scanning strategies are basically applied: rotation-only scanning with a cone beam, where the part is always inside the X-ray cone during the measurement rotation, and slice-wise scanning with fan-beam based CT systems, where the part is measured in sections of finite thickness during each part rotation, as commented in section 2.1.3.

More specifically, these are the scanning modes that could be done with CT:

- Rotation-translation scanning mode: the object is moved through the X-ray beam between fixed angles of the rotary table. This technique was applied in the beginning of industrial CT, nowadays it is rarely applied. It enables measuring large pieces but it requires longer times.
- Rotation-only scanning with offset: the object's center of rotation is displaced from the center of the X-ray beam. Then a part of the object is not inside the X-ray beam but enters the beam during rotation. It enables measuring large parts but it suffers from decreased resolution and accuracy.
- Rotation-only scanning with centered fan or cone beam: it is done with a full rotation of 360° , but it also can be done with rotations smaller than that value. A minimum of 180° is required. It should be noticed that smaller angular range decreases the measuring time, but worsens accuracy.
- Helical scanning: the relative movement of the X-ray source and detector to the object describes a helix. At first it was thought for medical applications, but recently this procedure has been readapted to industrial CT scanning. Helical scanning reduces measurement errors for those sides of the object which are parallel to the axis of rotation, however it needs more time in comparison to classical rotation-only cone beam scanning.

2.2.5 User influence

As there is a wide choice of measurement parameters and strategies, the user of the CT could be considered as an influence on the process itself.

Its influence starts with the system's warm up until the measurement begins, more specifically that interval of time where the thermal equilibrium of workpiece and CT system is achieved.

The parameterization of the measurement could be done by the user or by software expert systems, that way users of limited skill can operate CT systems with only a restricted choice in parameters.

The user influence is more evident when postprocessing is carried on, in terms of filtering, thresholding, and final geometrical analysis.

2.2.6 Threshold and noise

As a result of the CT scan an X-ray map absorption with its grey value profile is obtained. In general, it is impossible to extract dimensional and geometrical measurands from this kind of representation: the scan must be segmented, that means it needs an edge between the component and the environment, usually the surrounding air, this is done defining a threshold.

Threshold could be defined as the grey value of the voxel that differences a component from the surrounding air in the voxel representation of the measuring volume. This step would be easy, if the transition from the air to the component was sharp and perfect in the voxel representation. But this is not the case, in most situations the transition passes through several density values, due to the limitations of the reconstruction. In addition, the existence of artifacts like beam hardening may

make the measured density of the component inhomogeneous, or even worse the real density of the object can be inhomogeneous.

The choice of the wrong threshold leads to an over or underestimation of the dimensions of the component.

Noise is caused by quantization of X-ray photons itself, but can also be originated from many other noise sources, for example electronic noise of detector.

2.3 Sources of geometrical error

First, it is necessary to define the ideal situation in a CT scan. In this situation, there are no geometrical errors. It can be summarized as follows:

Firstly, the X-ray focal spot, the axis of the rotation, and the center of the detector should be in a plane; secondly, the straight line, which passes the focal spot and the detector center, should be vertical with the axis of rotation and the detector; thirdly, the axis of the rotation should be parallel to the row of the detector. Any deviations from these ideal conditions are considered influence factors and can contribute to errors in dimensional measurements.

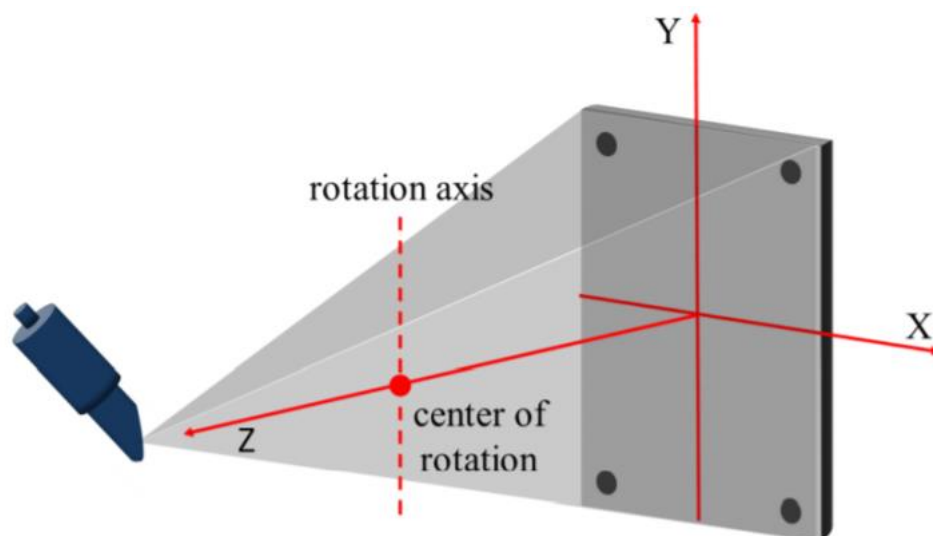


Figure 2-14: The ideal geometry of a CT system. (Valentina Aloisi, Simone Carmignato, Joseph Schlecht, Eric Ferley 2017)

To describe the ideal case, a right-handed system of Cartesian coordinates X , Y , and Z , is defined. As shown in Figure 2-14, the grey plane represents the planar detector, the center of the planar detector is the coordinate system origin, the X axis points to the ascending column direction, the Y axis points to the ascending row direction, and the Z axis is the normal of the detector and coincident with the central X-ray. The axis of the rotation intersects with the central X-ray. It is well known that no scanner system can be free from misalignments.

This section is going to be focused on explaining two main sources of geometrical error: angular misalignments of the detector and focal spot movement.

2.3.1 Angular misalignments of the detector

As seen before, no CT scan is free from misalignments, that includes the detector in the equation. Due to the assembly of the detector inside the CT machine, the detector can be tilted, slanted or skewed depending on the axis affected, see Figure 2-15.

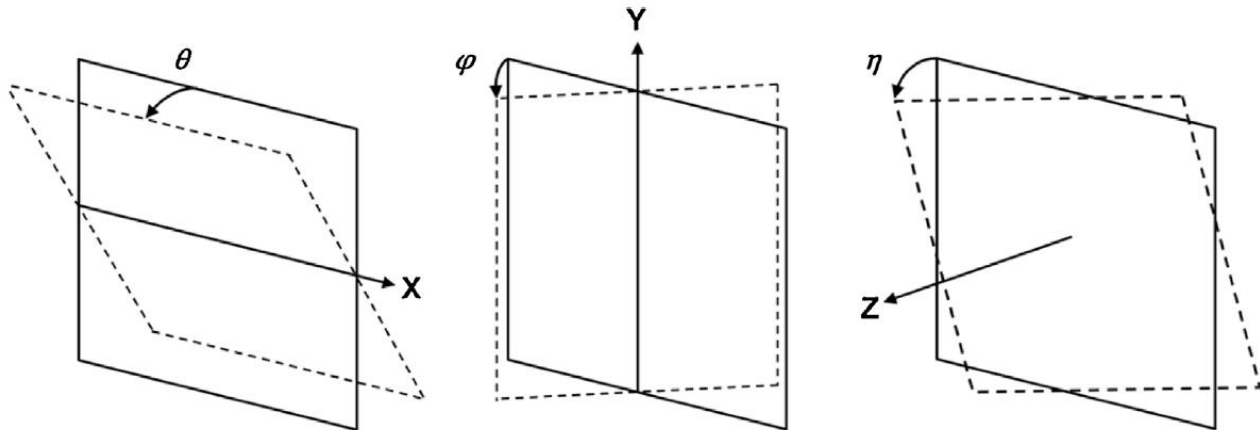


Figure 2-15: Potential detector angular misalignments including tilt θ (left), slant φ (middle), and skew η (right). Positive rotations are illustrated. (Massimiliano Ferrucci, Richard K Leach, Claudiu Giusca, Simone Carmignato and Wim Dewulf 2015)

These misalignments can be classified in two types: out-of-plane rotations, which include tilt and slant, and in-plane-rotations, which include skew.

It is unlikely to have just only one of those misalignments acting, usually it is a mix of them and not all of them affect in the same way the measurands, even when they are the same quantity. Therefore, the study of its effects gets harder.

A study done by, (Kumar J, Attridge A, Wood P K C and Williams M A 2011) made a research about the different effects that the misalignments of the detector produced in a 2mm Ball bar, see Figure 2-16.



Figure 2-16: Ball from study, (Kumar J, Attridge A, Wood P K C and Williams M A 2011).

In terms of skew, named as alpha in study, (Kumar J, Attridge A, Wood P K C and Williams M A 2011), the value tested was 0.4° , this resulted in length measurement errors up to 0.1%. The plot shows that errors from in-plane rotation increase as the ball bar is positioned away from the centre of the detector.

In terms of tilt, named as beta, the effect of deviation was more significant on the measurement of vertical distances and very little effect on horizontal distances.

Regarding the slant, named as gamma, it happened the opposite result, horizontal distances had higher errors than vertical lengths. For both tilt and slant, misalignments of 10° resulted in errors up to 1.5% of the measured length, depending on the position and orientation of the ball bar. The author explains that in-plane rotation can be solved by software and is not a critical misalignment.

On the other hand, the author suggests that detector tilt and slant should be aligned to within 1° to 2° from nominal.

Plots from the study are presented here, see Figure 2-17.

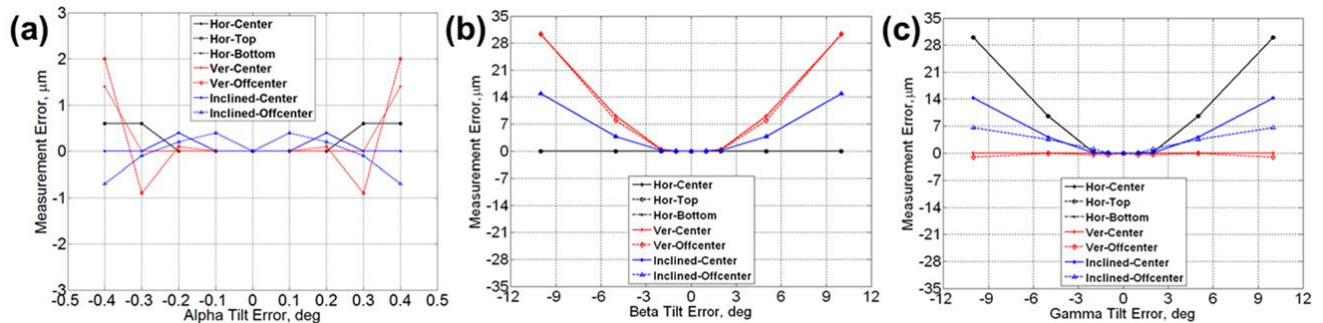


Figure 2-17: The error in measuring a 2-mm ball bar at various positions and orientations is plotted as a function of detector (a) in-plane rotation, (b) tilt, and (c) slant. (Massimiliano Ferrucci, Richard K Leach, Claudiu Giusca, Simone Carmignato and Wim Dewulf 2015).

Another study, (Wenig P and Kasperl S 2006) simulated the effects of geometrical errors on a reference object. In this study, the authors observed the effects of detector tilt, slant, and skew rotation. Each of the angles was individually deviated around 1° from their ideal value.

The average error for a group of seven independent distances on an alloy object, see Figure 2-18, was observed as a result of each misalignment separately. The results show that in-plane rotation of the detector created the largest average error in the measurement of the seven features (around 3.5% relative measurement error). The errors due to detector tilt and slant were barely noticeable.

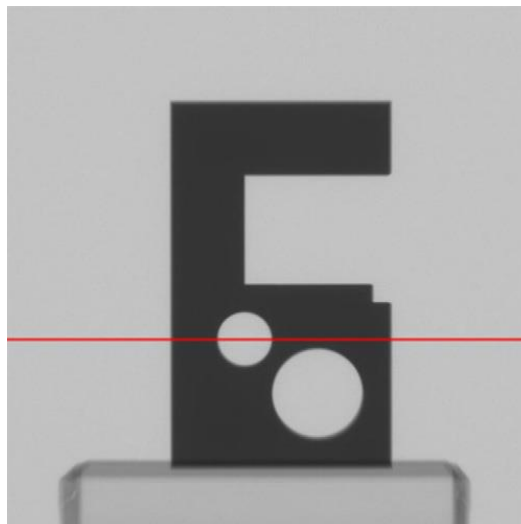


Figure 2-18: Object from study, (Wenig P and Kasperl S, 2006)

It is interesting to notice that the results of detector misalignment in this study, (Wenig P and Kasperl S 2006) are different to the results shown in (Kumar J, Attridge A, Wood P K C and Williams M A 2011). In, (Wenig P and Kasperl S, 2006), it is concluded that, for same angle of misalignment, 1° , in-plane rotation affected more the measurands than out-of-plane rotation. On

the other hand, in (Kumar J, Attridge A, Wood P K C and Williams M A 2011) the in-plane rotation is limited to 0.4° while the tilt and slant changes by 10° . It is then concluded, in (Kumar J, Attridge A, Wood P K C and Williams M A 2011), that tilt and slant have greater effects on measurement error than in-plane rotation.

It should be noted that test object in (Wenig P and Kasperl S 2006) includes various dimensional features (outer edges, inner edges, circle-to-circle distance, and circle diameter), some of which suffer from edge offsets caused by thresholding errors, whereas the object from (Kumar J, Attridge A, Wood P K C and Williams M A 2011), do not suffer from edge offsets.

It is concluded that observations of measurement error depend strongly on the object tested.

2.3.2 Focal spot movement

As X-ray source operates, it releases heat that results in a change in the geometrical features of the X-ray tube due to heat expansion and inner vibration, which can be manifested as a movement, or drift, of the focal spot. This movement leads to deviations in the imaging geometry, as introduces errors in the image reconstruction process and affects the accuracy of dimensional measurements, (Curry T S, Dowdey J E and Murr R E 1990).

The influence of focal spot movement on the positional stability of 2D projections was investigated experimentally and by computer simulation, (Hiller J, Maisl M and Reindl L M 2012), (Vogeler F, Verheecke W, Voet A and Kruth J 2011), (Reisinger S, Schmitt M and Volland V 2012), (Fröba T and Steffen J P 2011), (Steffen J P and Fröba T 2011), (Weiss D, Deffner A and Kuhn C 2010), (Uhlman N, Salamon M, Burtzlauff S, Porsch F, Johansson W, Nachtrab F and Hanke R 2008). Experimental methods are basically based on observing the drift in the 2D projections of a stationary reference object in time. These reference objects include a small metal sphere, (Hiller J, Maisl M and Reindl L M 2012), calibrated ruby spheres (Weiss D, Deffner A and Kuhn C 2010), a calibrated hole plate (Vogeler F, Verheecke W, Voet A and Kruth J 2011) and a cross wire, (Uhlman N, Salamon M, Burtzlauff S, Porsch F, Johansson W, Nachtrab F and Hanke R 2008). Specific characteristics of the reference object are determined in each projection and the change in position of the feature between scans is calculated, considering that all this variation in position is due to the movement of the focal spot.

In (Fröba T and Steffen J 2011), authors developed a different procedure to measure focal spot movement. Here, the focal spot movement was obtained from the length change of the X-ray tube which was measured using a micrometer gauge.

It is difficult to perform a comparison of the results between the different methods, since the studies were carried out using different CT systems with a variety of experimental set-ups. Nevertheless, a few conclusions about focal spot movement can be summed up from those studies:

- A shift in the position of reference object in 2D projections was evident in all reported experiments.
- The largest shift in 2D projections took place in the first few minutes of the experiment, as at the first minutes, the variation of temperature in time was the highest.
- Increasing the power of the X-ray source augments the magnitude of the focal spot movement, (Weiss D, Deffner A and Kuhn C 2010).

Study (Vogeler F, Verheecke W, Voet A and Kruth J 2011) noticed a repeatable behaviour of the focal spot movement, where the focal spot drift was the main cause to the positional instability of

2D projections. Study (Hiller J, Maisl M and Reindl L M 2012) found out that the movement was linear with sinusoidal oscillations.

Another study, (Nadia FLAY, Wenjuan SUN, Stephen BROWN, Richard LEACH, Thomas BLUMENSATH 2015) made a research of the focal spot drift and its correlation with thermal properties of a CT system. To observe the drift of the focal spot in the CT system, some reference objects were designed specifically to minimise the number of factors that can influence the positional stability of 2D projections. There were two different procedures applied, cold and hot scans. Each cold scan gathers 3142 projections and each hot scan gathers 10000 projections.

These were the conclusions:

- The focal spot movement existed in all scans.
- For all cold scans, the movement of the (x,y) centre coordinates in the x-axis did not surpassed 0.15 pixels (30 μm), approximately 0.25 μm drift of the focal spot. The movement in the y-axis did not surpassed 0.4 pixels (80 μm), about 0.6 μm drift of the focal spot.
- In cold scans most of the movement in both axes happened during the initial eight to ten minutes. It can be concluded that the observed movement is due to the instability of the focal spot as the temperature inside the X-ray source augments. It is recommended for the user to identify the behaviour of the focal spot movement in their particular X-Ray system and also to allow the X-ray source stabilising for an appropriate period of time before image extraction.

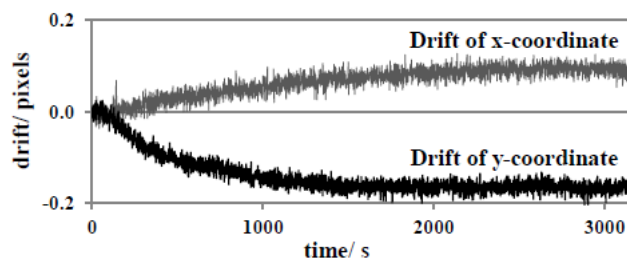


Figure 2-19: Drift in the (x,y) centre coordinates in cold scan. (Nadia Flay, Wenjuan Sun, Stephen Brown, Richard Leach, Thomas Blumensath 2015).

- For all hot scans, the magnitude of the movement of the (x,y) centre coordinates did not surpassed 0.1 pixels (20 μm) in both axes, about 0.15 μm movement of the focal spot. Such small value of the drift could be considered at the levels of the noise of the system.
- Additionally, no trend of drift direction was observed in hot experiments. The start direction of the drift looks to be random but once the direction was initiated, the movement kept on in that direction.

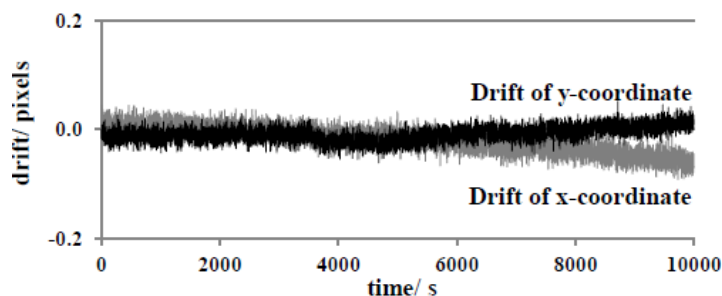


Figure 2-20: The drift in the (x,y) centre coordinates in hot scan. (Nadia Flay, Wenjuan Sun, Stephen Brown, Richard Leach, Thomas Blumensath 2015).

2.4 Measurement uncertainty in CMM

The definition of uncertainty is: parameter, associated with the result of a measurement, that characterizes the dispersion of the values that could reasonably be attributed to the measurands. Complete measurement reports must contain statement about the measurement uncertainty. Uncertainty is relevant due to two important metrological concepts: decision on "the acceptance or rejection" and maintaining traceability in accordance with ISO 9000 standards, (International Organization for Standardization 1998), (Trapet, E., Savio, E., De Chiffre, L. 2004).

When it comes to the evaluation of the measurement uncertainty in CMMs, there are many uncertainty sources that need to be considered. One possible classification of those sources of uncertainty is given in Figure 2-21.

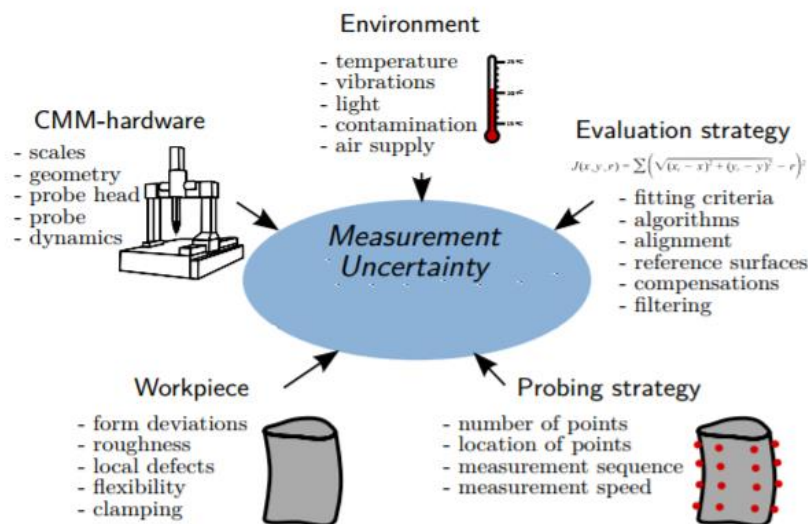


Figure 2-21: Classification of sources of uncertainty. (Nick Van Gestel, 2011)

- **Hardware:** uncertainty related with the hardware components of the CMM like probe uncertainty.
- **Environment:** mostly temperature but not only as temperature deviations from 20°C, but also as temperature gradients, in time and space that will influence the measurement uncertainty, (J.P. Kruth, P. Vanherck, and C. Van den Bergh, 2001). In addition, there exist other environmental influences that affect uncertainty like vibrations, non-constant air supply, when using air bearings, and lighting conditions, in case that optical probing systems are used.
- **Workpiece:** most part of uncertainty comes from form deviations, but also surface imperfections like roughness and local defects, such as burrs and scratches, can affect. Even deformations due to probing forces or clamping play a role.
- **Probing strategy:** determines the amount of measurement points and their location. Indeed, the measuring sequence and settings like measurement velocity can be important. The more complex the probing system is, the more parameters will influence the measurement uncertainty.

- Evaluation Strategy: includes the type of fitting criteria, algorithm precision, filtering, alignment strategy, selected reference surfaces...

In order to evaluate the measurement uncertainty of the CMM used, there are three types of methods to do it:

- Use of multiple measurements strategies without calibrated workpieces or standards (ISO/TS 15530-2): the measurement is done multiple times, enabling to determine the repeatability and reproducibility of the measurement. Measurement repeatability is obtained during constant measurement conditions whereas measurement reproducibility is obtained while changing measurement conditions. They are independent of the true value of the measurand, which is an advantage, since the true value is unknown. Nevertheless, there is a clear disadvantage in this first method because as systematic errors are not taken into consideration, no upper limit for the measurement uncertainty is provided. This method provides only a lower limit for the measurement uncertainty and is only useful when no other ways to determine measurement uncertainties are available.
- Use of multiple measurements strategies with calibrated workpieces (ISO/TS 15530-3 2004): the measurement is done multiple times too, but in this case a calibrated workpiece is used as test object. The calibrated object used and environment conditions during the uncertainty evaluation should be similar as in the actual measurement. The errors measured during the uncertainty evaluation with the calibrated workpiece are used to determine measurement uncertainties for actual measurements. Since this method makes use of calibrated workpieces it also accounts for systematic measurement errors. This is a very reliable method to determine measurement uncertainty, but it is usually very expensive and time consuming, (J.M. Baldwin, K.D. Summerhays, D.A. Campbell, and R.P. Henke 2004).
- Use of computer simulation (ISO/TS 15530-4 2004), (ISO 4288:1996 1996): the measurement is simulated multiple times. The simulation is based on a mathematical model of the measurement process and considers all important influence quantities. During simulation, these influence quantities are changed in their likely ranges. This results in variations on the simulated measurement results. The dispersion on the simulated measurement results is used to determine the measurement uncertainty. Since this is a non-experimental approach, it is much faster and cheaper. The main problem relies in finding a mathematical model that incorporates all influence quantities.
- Use of expert judgement: probably the most popular method to determine measurement uncertainties. Measurement uncertainties are calculated based on knowledge and experience of a CMM expert. Depending on the complexity of CMM measurements, expert judgement will not always be reliable and is only recommended when no other methods are applicable.

3 State of the art

3.1 Previous methods for geometrical error estimation

In most literature about methods for geometrical error estimation, the methods can be divided into two types, as presented in Figure 3-1.

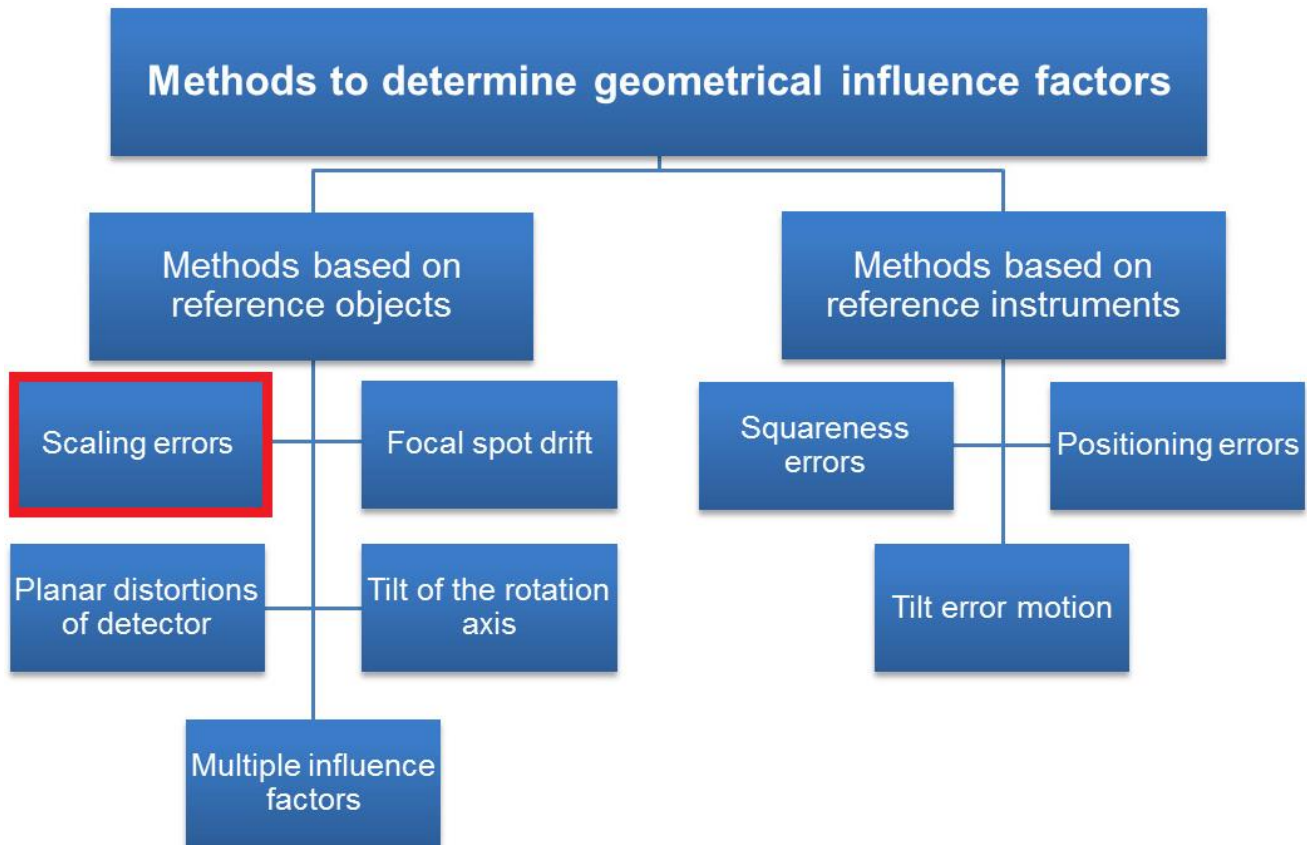


Figure 3-1: The methods to determine geometrical influence factors are separated into two categories: Methods based on the use of reference objects (also known as imaging methods) and the methods based on the use of reference instruments. Adapted from (Massimiliano Ferrucci, Richard K Leach, Claudiu Giusca, Simone Carmignato and Wim Dewulf 2015).

The first type examines the geometry for a static position of the rotation platform. Basically, the reference object is imaged and the imaging geometry is obtained from the projection data, or from the voxel data. These methods are known as imaging methods. It is important to notice that these imaging methods are only valid for fixed positions of the rotation stage, when the position of the rotation stage varies, the geometry must be evaluated again.

The second type of methods takes into account error motions of the kinematic mechanisms. They are based on the use of reference instruments, like laser interferometers and electronic levels, to measure kinematic behaviours.

In terms of determine scale errors, the usually methods scan a reference object, which has a series of calibrated length segments, and subsequently re-scale the voxels with the difference between the lengths measured by CT and their corresponding calibrated values.

As a state of the art the study, (Muller P 2012) from DTU is very important for this thesis. Here, a carbon-fibre plate with twenty-five ruby spheres arranged in a regular grid pattern was used as a reference object, this reference object served as model for the reference object of this thesis, see Figure 3-2.



Figure 3-2: Ball Plate from DTU. (Muller P 2012)

The distances between sphere centres, for all possible pair of spheres, were calibrated, then the distance between sphere centres was measured by CT. The authors estimated the deviation, or measurement error, of each CT length measurement from its calibrated reference value. Sphere distance errors were represented against their corresponding calibrated values, see Figure 3-3.

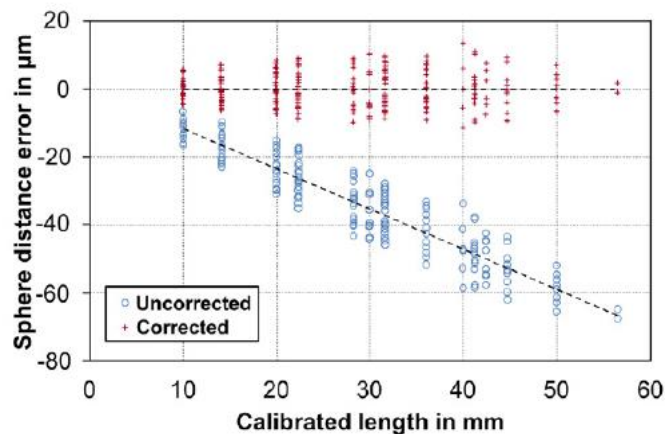


Figure 3-3: Plot. (Muller P 2012)

A linear regression fit was applied to the sphere distance error, see Equation 3-2, and the slope of the regression line, a , was used to correct the voxel scale, see Equation 3-1. S_{VOX} is the correction factor to be applied to the original voxel scale.

The voxels were corrected and the residual sphere distance errors, see Equation 3-3, were plotted against their corresponding calibrated values, see Figure 3-3.

$$S_{VOX} = \frac{1}{a+1} \quad \text{Equation 3-1}$$

$$SD_{uncor} = L_{CT} - L_{CMM} \quad \text{Equation 3-2}$$

$$SD_{cor} = SD_{uncor} + a * L_{CMM} \quad \text{Equation 3-3}$$

Another state of the art for this thesis could be the study by (Jintao Zhao, Xiaodong Hu, Jing Zou and Xiaotang Hu 2015). The authors of this study proposed an iterative method to estimate nine parameters that described the geometry of the system.

To do the estimation, the authors designed a TPB (Two-Piece-Ball represents two flat planes with nine ruby balls in each plane) phantom. The advantage of this method was that only one single projection of the phantom at one angle every time was required and the corresponding parameters were derived from that projection. In some previous studies, authors always considered seven parameters to describe the geometry of the system. However, in this study nine were of them were considered, these two additional parameters were offsets of the X-ray source spot. Normally, in previous studies, these two errors were always converted to errors of the detector. However, if the phantom was in a plane or taking the focal spot drifts into consideration this conversion would be inexact. Additionally, the authors designed an adjusting mechanism to adjust the location of the detector. The angle of the detector would be adjusted every time basing on the calibration parameters until it approached zero or matched their needs.

Normally, three times was enough to adjust the system to a relatively ideal condition.

As said before, in this method they considered nine parameters: (1) μ_1 and v_1 detector offsets along X and Z axis; (2) α angle of detector tilt around X axis; (3) β angle of detector tilt around Z axis; (4) γ angle of detector tilt around Y axis; (5) μ_2 and v_2 X-ray source offsets along X and Z axis; (6) SOD distance between X-ray source and rotation axis, estimated value referred as f ; (7) SDD perpendicular distance from X-ray source to detector.

To determine the parameters, they used some mathematical formulas, supposedly obtained from the Euclidian distances between balls of the phantom but no explanation to the formulas was given in the text, that is the main reason why the application of this method in this thesis was neglected, see Figure 3-4.

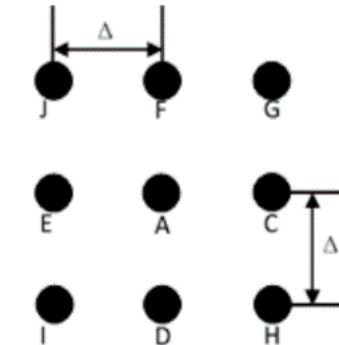


Figure 3-4: Phantom. (Jintao Zhao, Xiaodong Hu, Jing Zou and Xiaotang Hu 2015)

The authors thought that the ratio of distances between projections from spheres IJ and HG influenced the angle of β . The ratio of distances between projections of AC, AE and AF, AD, influenced α and β , and the coordinates of the centers of the projected spheres D and F affected γ .

First, they obtained parameters a , b and c as a ratio between spheres distances, see Equations 3-4, 3-5 and 3-6. In equation 3-6 the parameter l is equal to two times the distance Δ .

$$\frac{|A_0C_0|}{|A_0E_0|} = \frac{Y_s - Y_A - \cos\alpha * \sin\beta * \Delta}{Y_s - Y_A + \cos\alpha * \sin\beta * \Delta} = a \quad \text{Equation 3-4}$$

$$\frac{|A_0D_0|}{|A_0F_0|} = \frac{Y_s - Y_A + \sin\alpha * \Delta}{Y_s - Y_A - \sin\alpha * \Delta} = b \quad \text{Equation 3-5}$$

$$\frac{|I_0J_0|}{|H_0G_0|} = \frac{2*f+l*\tan\beta}{2*f-l*\tan\beta} = c \quad \text{Equation 3-6}$$

Then, when those ratios were obtained, authors determine slant, tilt and skew with Equations 3-7, 3-8 and 3-9.

$$\beta = \arctan\left(\frac{f*(c-1)}{\Delta*(c+1)}\right) \quad \text{Equation 3-7}$$

$$\alpha = \arctan\left(\sin(\arctan(\beta)) * \frac{a+1}{1-a} * \frac{b-1}{b+1}\right) \quad \text{Equation 3-8}$$

$$\tan\gamma = \frac{X_{F_0} - X_{D_0}}{Z_{D_0} - Z_{F_0}} \quad \text{Equation 3-9}$$

Then, it was possible to obtain offsets from detector, μ_1 and ν_1 , with Equation 3-10 and 3-11.

$$\begin{aligned} & [\sin\alpha \cdot \sin\beta \cdot \sin\gamma \cdot Y_S - \cos\beta \cdot \cos\gamma \cdot Y_S - \cos\alpha \cdot \sin\beta \cdot X_S] \cdot \mu_1 + [\cos\alpha \cdot \sin\gamma \cdot Y_S + \sin\alpha \cdot X_S] \cdot \nu_1 \\ & = (Y_S - Y_A) \cdot X_{A_0} - (SDD - SOD) \cdot [\sin\beta \cdot \cos\gamma \cdot Y_S + \sin\alpha \cdot \cos\beta \cdot \sin\gamma \cdot Y_S - \cos\alpha \cdot \cos\beta \cdot X_S] \\ & [-\sin\alpha \cdot \sin\beta \cdot \cos\gamma \cdot Y_S - \cos\beta \cdot \sin\gamma \cdot Y_S - \cos\alpha \cdot \sin\beta \cdot Z_S] \cdot \mu_1 + [-\cos\alpha \cdot \cos\gamma \cdot Y_S + \sin\alpha \cdot Z_S] \cdot \nu_1 \\ & = (Y_S - Y_A) \cdot Z_{A_0} - (SDD - SOD) \cdot [\sin\beta \cdot \sin\gamma \cdot Y_S - \sin\alpha \cdot \cos\beta \cdot \cos\gamma \cdot Y_S - \cos\alpha \cdot \cos\beta \cdot Z_S] \end{aligned}$$

$$\text{Equation 3-10 and 3-11}$$

Where X_{A_0} , Z_{A_0} were obtained from Equation 3-12 and represented the coordinates from the projection of sphere A in X and Z axis.

$$\begin{aligned} X_{A_0} &= \frac{Y_S \cdot X_A - Y_A \cdot X_S}{Y_S - Y_A} \\ Z_{A_0} &= \frac{Y_S \cdot Z_A - Y_A \cdot Z_S}{Y_S - Y_A} \end{aligned}$$

$$\text{Equation 3-12}$$

Then, it was the moment to calculate the variation of the offset Δu and Δv .

$$\begin{aligned} DF^2 &= \frac{4 \cdot (Y_S - Y_A)^2 \cdot \Delta^2}{[(Y_S - Y_A)^2 - (\sin\alpha \cdot \Delta)^2]} \cdot \{ [X_{A_0} \cdot \sin\alpha - (u_2 - u_1) \cdot \sin\alpha \cdot \cos\beta - SDD \cdot \sin\alpha \cdot \sin\beta]^2 \\ &+ [Z_{A_0} \cdot \sin\alpha + (v_2 - v_1) \cdot \sin\beta - SDD \cdot \cos\beta]^2 \} \end{aligned}$$

$$\text{Equation 3-13}$$

When Δu and Δv were known, Equation 3-14 was applied to obtain μ_2 and ν_2 .

$$D_1 F_1^2 = \frac{4 \cdot (Y_S - Y_A)^2 \cdot \Delta^2}{[(Y_S - Y_A)^2 - (\sin \alpha \cdot \Delta)^2]} \cdot \{ [X_{A_0} \cdot \sin \alpha - (u_2 - u_1) \cdot \sin \alpha \cdot \cos \beta - SDD \cdot \sin \alpha \cdot \sin \beta]^2 + [Z_{A_0} \cdot \sin \alpha + (v_2 - v_1) \cdot \sin \beta - SDD \cdot \cos \beta]^2 \}$$

Equation 3-14

Where, $Z_{A_{10}}$ and $X_{A_{10}}$, were calculated with Equation 3-15:

$$X_{A_{10}} = \frac{Y_S \cdot X_A - Y_A \cdot X_S}{Y_S - Y_A} = \frac{Y_S \cdot (X_A - \sin \beta \cdot \cos \gamma \cdot \Delta - \sin \alpha \cdot \cos \beta \cdot \sin \gamma \cdot \Delta) - X_S (Y_A - \cos \alpha \cdot \cos \beta \cdot \Delta)}{Y_S - Y_A + \cos \alpha \cdot \cos \beta \cdot \Delta}$$

$$Z_{A_{10}} = \frac{Y_S \cdot Z_A - Y_A \cdot Z_S}{Y_S - Y_A} = \frac{Y_S \cdot (Z_A - \sin \beta \cdot \sin \gamma \cdot \Delta + \sin \alpha \cdot \cos \beta \cdot \cos \gamma \cdot \Delta) - Z_S (Y_A - \cos \alpha \cdot \cos \beta \cdot \Delta)}{Y_S - Y_A + \cos \alpha \cdot \cos \beta \cdot \Delta}$$

Equation 3-15

The whole process could be summed up like appears in Figure 3-5.

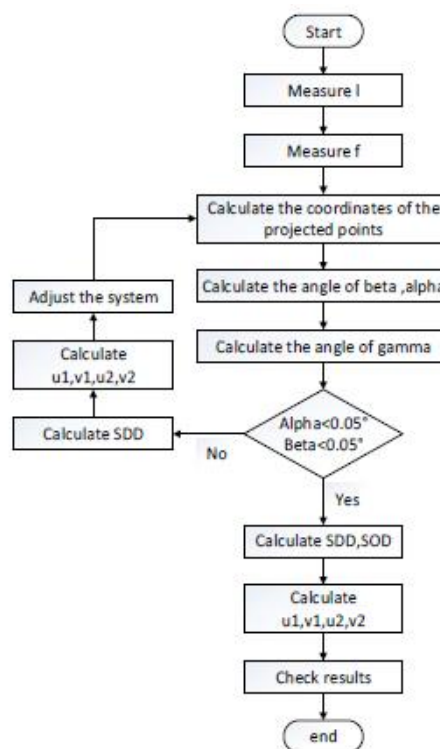


Figure 3-5. (Jintao Zhao, Xiaodong Hu, Jing Zou and Xiaotang Hu 2015)

In terms of the angular misalignments of the detector, is interesting to stand out the recent study, (Valentina Aloisi, Simone Carmignato, Joseph Schlecht, Eric Ferley 2017). In this work, the authors studied experimentally the effects of detector misalignment on a metrology CT system, more specifically in a NSI CXMM50. As a reference object, they used a ball bar consisting of seven

equally spaced spheres with distances ranging from 5mm to 30mm, previously calibrated in a CMM.

Then, the flat-panel detector was physically misaligned in order to examine the effect of a detector out-of-plane rotation about the X axis on the measurement result, see Figure 3-6.

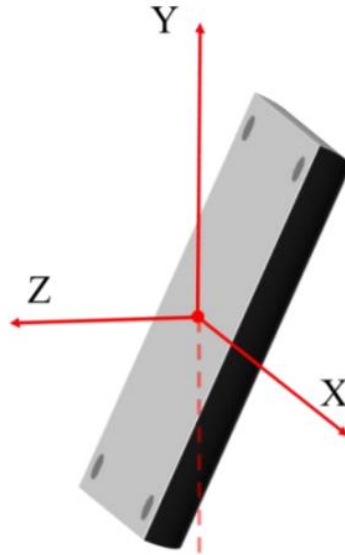


Figure 3-6: Tilted detector about the X axis. (Valentina Aloisi, Simone Carmignato, Joseph Schlecht, Eric Ferley 2017)

They chose three angular misalignments of approximately 0.5° , 1° and 1.5° , which were reasonable values as they were smaller than those easily eliminated by mechanical assembly.

For each angle configuration, one scan was obtained with the ball bar placed vertically, as this direction was expected to be the most critical for results when there is tilt in X axis, (Kumar J., Attridge A., Wood P. K. C., Williams M. A. 2011), and positioned off-center from the center of rotation.

The ball bar was positioned in a way that the middle sphere, number 4, was approximately centered on the middle plane of the detector in the ideal configuration; number 1 was placed close to the level of the upper edge of the detector and number 7 was placed close to the height of the lower edge of the detector.

As a result, the sphere center-to-center measurement errors, calculated as the difference between CT measured values and CMM reference values, were represented for each of the six nominal lengths of the ball bar in the different scenarios, see Figure 3-7.

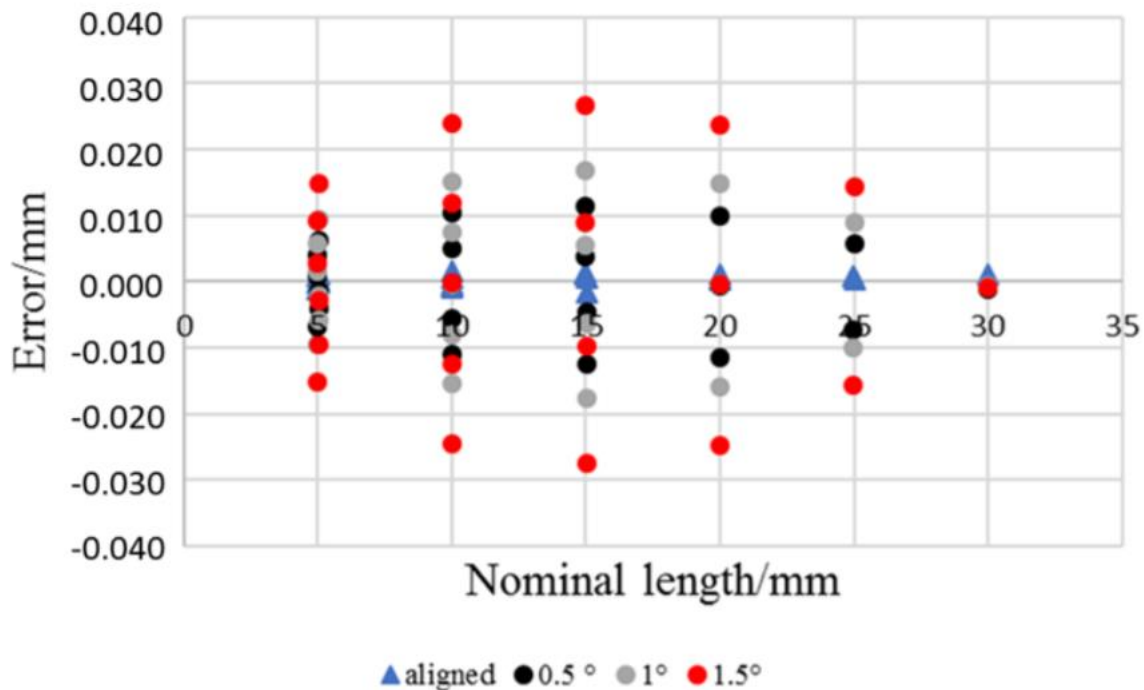


Figure 3-7: Sphere distance errors for all the six nominal lengths of the ball bar. (Valentina Aloisi, Simone Carmignato, Joseph Schlecht, Eric Ferley 2017)

As expected, the angular misalignment had a strong influence on the results. With a misalignment of approx. 0.5° about the X axis sphere center-to-center errors got up to $12\ \mu\text{m}$. When increasing up to 1° the sphere center-to-center errors reached $18\ \mu\text{m}$. The worst case was at 1.5° misalignment which led to $28\ \mu\text{m}$ in sphere distance errors.

When analysing the effects of the different misalignment angles on the diameter errors of the spheres of the ball bar, it was clear to see that the spheres in similar regions on the detector, but at opposite sides, presented equal diameter errors but with opposite sign. Additionally, when increasing the angular misalignment, the measured diameter errors increased. For a 1.5° misalignment error rose up to $5.3\ \mu\text{m}$ for sphere number 1. It would be interesting to see that sphere no.4, which was approximately in the center of the detector, was nearly non-affected by the misalignments. In the aligned configuration, there was no trend in diameter error and all the errors were occasionally from zero to $2\ \mu\text{m}$. Therefore, the results shown in Figure 3-8 were caused by the angular misalignment about the X axis.

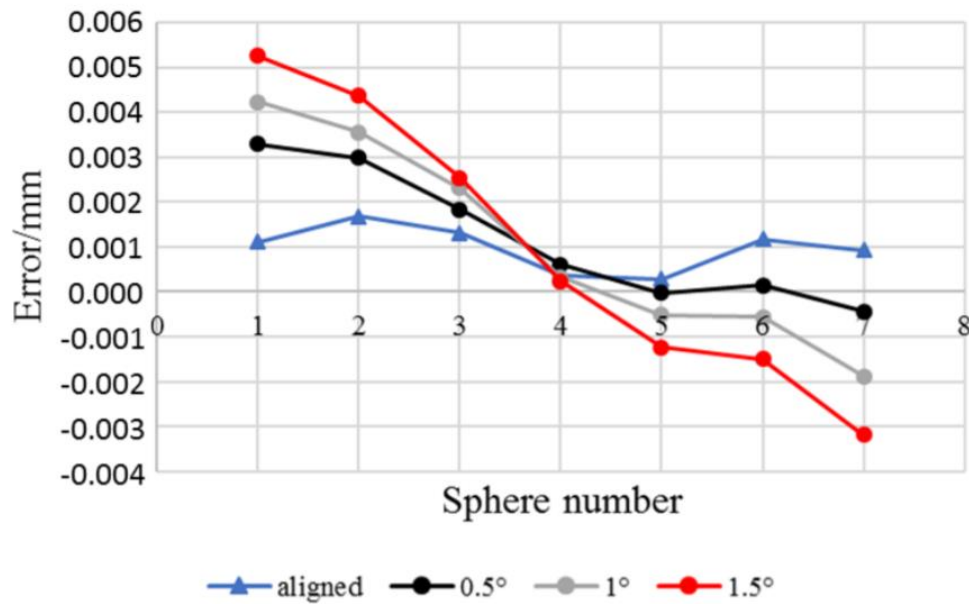


Figure 3-8: Diameter errors for the seven spheres of the ball bar. (Valentina Aloisi, Simone Carmignato, Joseph Schlecht, Eric Ferley 2017)

3.2 Reference objects

As mentioned before in section 3.1 some methods to determine geometrical influence factors need a reference object in the process. Those elements are of vital importance when doing imaging methods. There is a wide variety of them as presented in study, (Muller P 2012).

There are a lot of different reference objects which have been developed for determination of specific errors in CT. So, that each reference object fits for a particular estimation of a specific error in CT, obviously, there are some objects that can be used for more than one type of error.

In order to correct scale errors, commonly used objects are those consisting of spheres made of different materials, preferably ruby, alumina, zirconia and steel, allowing point-to-point distance measurements, see Figure 3-2 and Figure 3-9, and those with features like holes, such as calotte plates and hole plates, see Figure 3-10. Usually, these objects are attached to carbon fibre rods or carbon fibre plates. Carbon fibre is a widely-used material in CT applications due to its high penetrability to X-rays and since it does not originate no image artifacts in the reconstructed volume, as it would be seen in the results from this thesis in section 4.

The measurand between spheres centres or holes axes, respectively, measured on CT systems is nearly independent from the threshold applied. This makes the evaluation of scaling factors very robust and independent from threshold determination, (S. Carmignato 2007). Nevertheless, due to manufacturing processes issues it is more preferred to use reference objects containing spheres rather than hole plates or calotte plates, as the precision of the latter ones, in terms of precise hole axis positioning, is more likely to be lower.

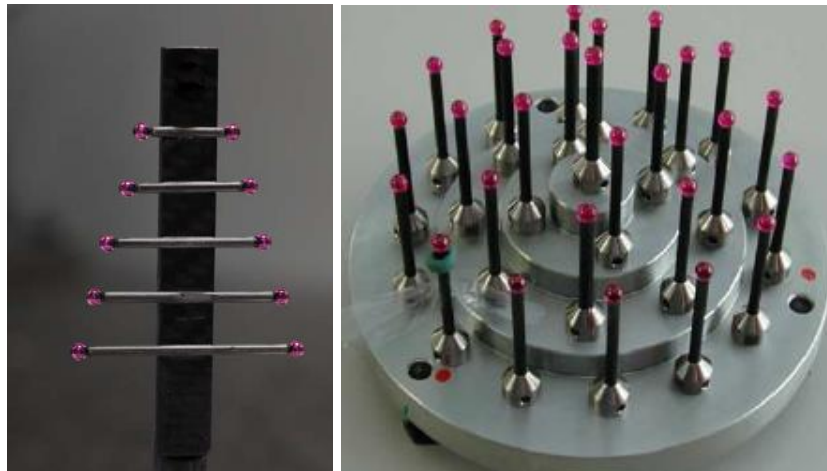


Figure 3-9: (a) CT Ball Tree, (b) Invar 27 Sphere gauge. (Müller, Pavel 2010)

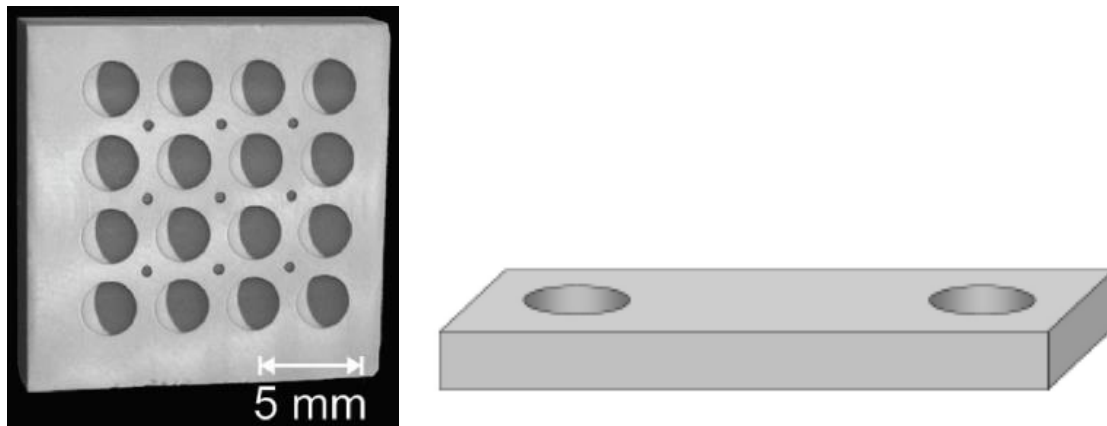


Figure 3-10: (a) Calotte Plate and (b) Hole Bar. (Müller, Pavel 2010)

Threshold value, is evaluated by measurement of internal and external features. The dimensions of inner and outer characteristics depend on changing threshold in one way or another. If threshold value increases, dimensions of inner features augment whereas dimensions of outer features decrease and vice versa. By using a calibrated reference object, the correct threshold value is determined as the value that reduces the maximum between: deviation of inner dimension compared to its calibrated value, and deviation of outer dimension compared to its calibrated value. Therefore, threshold value is an important factor for surface determination and accuracy of dimensional measurements.

These objects could be: hole bars, see Figure 3-10 (b), hollow cylinders, fibre gauge, see Figure 3-11, step cylinders with or without central hole, see Figure 3-12, and pan flute gauge, see Figure 3-13.

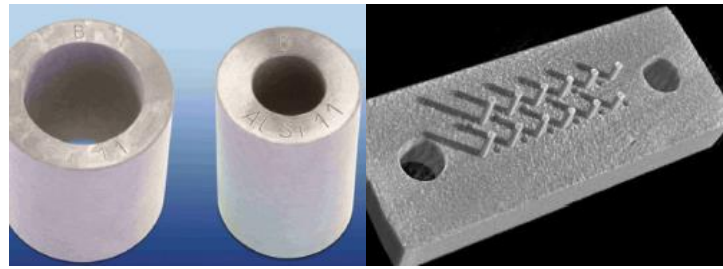


Figure 3-11: (a) Hollow cylinders and (b) Fibre gauge. (Müller, Pavel 2010)



Figure 3-12: (a) Step cylinders with central hole and (b) without central hole. (Müller, Pavel 2010)

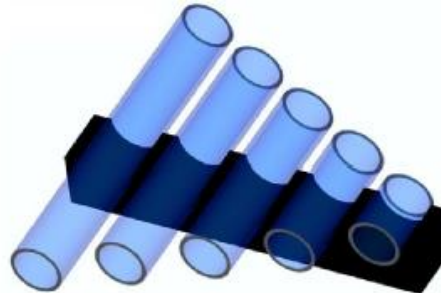


Figure 3-13: Pan flute gauge. (Müller, Pavel 2010)

As mentioned in section 2.2.1, in order to correct beam hardening some reference objects can be used. These objects would be: step wedge, see Figure 3-14, step cylinder with bore hole and step cylinder without bore hole, see Figure 3-12.

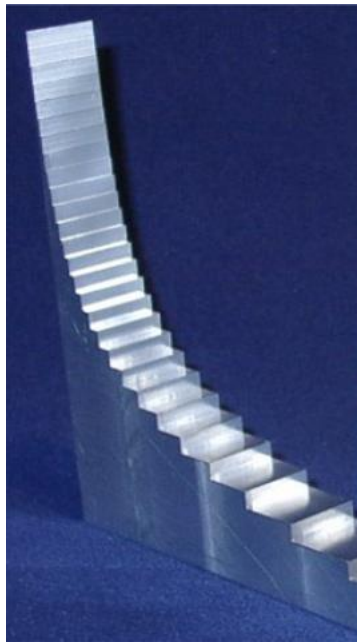


Figure 3-14: Step wedge. (Müller, Pavel 2010)

As state of the art, it is interesting to mention the CT Ball Plate, see Figure 3-2. This reference object was designed in DTU for the study, (Muller P 2012) and served as a reference for developing the reference object of this thesis. The object featured a regular 5x5 matrix of ruby spheres, which were glued on a carbon fibre plate. The general concept of the CT ball plate was similar to the conventional ball plates, (H. Kunzmann, E. Trapet, F. Wäldele 1995) and hole plates, (H. N. Hansen, L. De Chiffre 1997), (L. De Chiffre, H. N. Hansen, R. E. Morace 2005) used in classical coordinate metrology.

It was a multi-purpose reference object as it could be used for: performance characterization of industrial CT scanners, determination of measuring errors in the CT volume and geometrical correction of CT data like scale error (Muller P 2012).

4 Own approach

4.1 Development of CT Ball Plate

As commented in section 3.2 the reference object used for this thesis was a Ball Plate. It will be named from now on as CT Ball Plate.

This reference object was composed of a Carbon Fibre Reinforced Polymer (CFRP) plate of 52x52x4mm and twenty-five Ø3mm Ruby Spheres G5. In DIN5401/ISO 3290 the quality G5 means a sphericity of 0,13 µm, see Figure 4-1 for more details about DIN5401.

DIN 5401 : 2002-08 (GERMAN STANDARDS)

GRADE	Class	Nominal diameter Dw (mm)		Limit deviations (µm) (5)	Ball diameter variation	Roundness error	Surface roughness (R)	Lot diameter variation (5)	Subgauge interval	Subgauges (µm) (7)		
		From	To		VDws Max. (µm)	TDws Max. (µm)	Ra Max. (µm)	VDwt./A Max. (µm)	IG, ST (µm)			
G3	-	-	12.7	± 5,32	0.08	0.08	0.010	0.13 (L)	0.5	from -5 to -0.5	0	from +0.5 to +5
G5	I	-	12.7	± 5,63	0.13	0.13	0.014	0.25 (L)	1	from -5 to -1	0	from +1 to +5
G10	II	-	25.4	± 9,75	0.25	0.25	0.020	0.50 (L)	1	from -9 to -1	0	from +1 to +9
G16 (1)	II	-	25.4	± 11,4	0.40	0.40	0.025	0.80 (L)	2	from -10 to -2	0	from +2 to +10
G20 (1)	III	-	38.1	± 11,5	0.50	0.50	0.032	1.0 (L)	2	from -10 to -2	0	from +2 to +10
G28 (1)	III	-	50.8	± 13,7	0.70	0.70	0.050	1.4 (L)	2	from -12 to -2	0	from +2 to +12
G40	III	-	100	± 19,0	1.0	1.0	0.060	2.0 (L)	4	from -16 to -4	0	from +4 to +16

Figure 4-1: DIN 5401. Adapted from (Reiff GmbH)

These spheres were disposed in a 5x5 matrix with a nominal distance between sphere centres of 8mm and a tolerance due to manufacturing process of ±0,005mm. Additionally, there was a tolerance of perpendicularity between the lines that connected all holes centres, in vertical and horizontal direction.

This CT Ball Plate offered exactly ninety-three precise measurands between sphere centers, taking into account all possible couples of spheres which were in the same row or in the same column without repeating any combination of spheres. That means for example that the measurand between sphere no.18 and sphere no.19 was performed just one time per measurement, either from no.18 to no.19 or from no. 19 to no.18.

The nominal values existent, in the different ninety-three combinations, were: 8mm, 16mm, 24mm and 32mm. More specifically, there were: thirty-six combinations with a nominal value of 8mm, twenty-eight combinations with a nominal value of 16mm, nineteen combinations with a nominal value of 24mm and ten combinations with a nominal value of 32mm.

Regarding the manufacture of the plate, the 52x52mm plate was cut from a bigger plate by water jet cutting process, this process was done by Mössinger WaterWorxx GmbH. The holes of the plate were done at the WBK-Workshop. In order to enhance the grip of the spheres in the plate, it was decided to use truncated conical holes, whose manufacturing steps are shown below.

First, a cylindrical hole of 0,5mm diameter, without precise tolerance needed, was made with a cylindrical drill reaching a depth of 2,5 mm approx. Second, with the countersink, a truncated conical hole was made with 2,5mm diameter on top, a chamfer angle of 90° and a depth of 1mm with a tolerance of $\pm 0,005$ mm, see Figure 4-2.

The spheres were named with a number from 1 to 25 in a laevorotatory helix beginning at the low-left corner of the plate, see Figure 4-3.

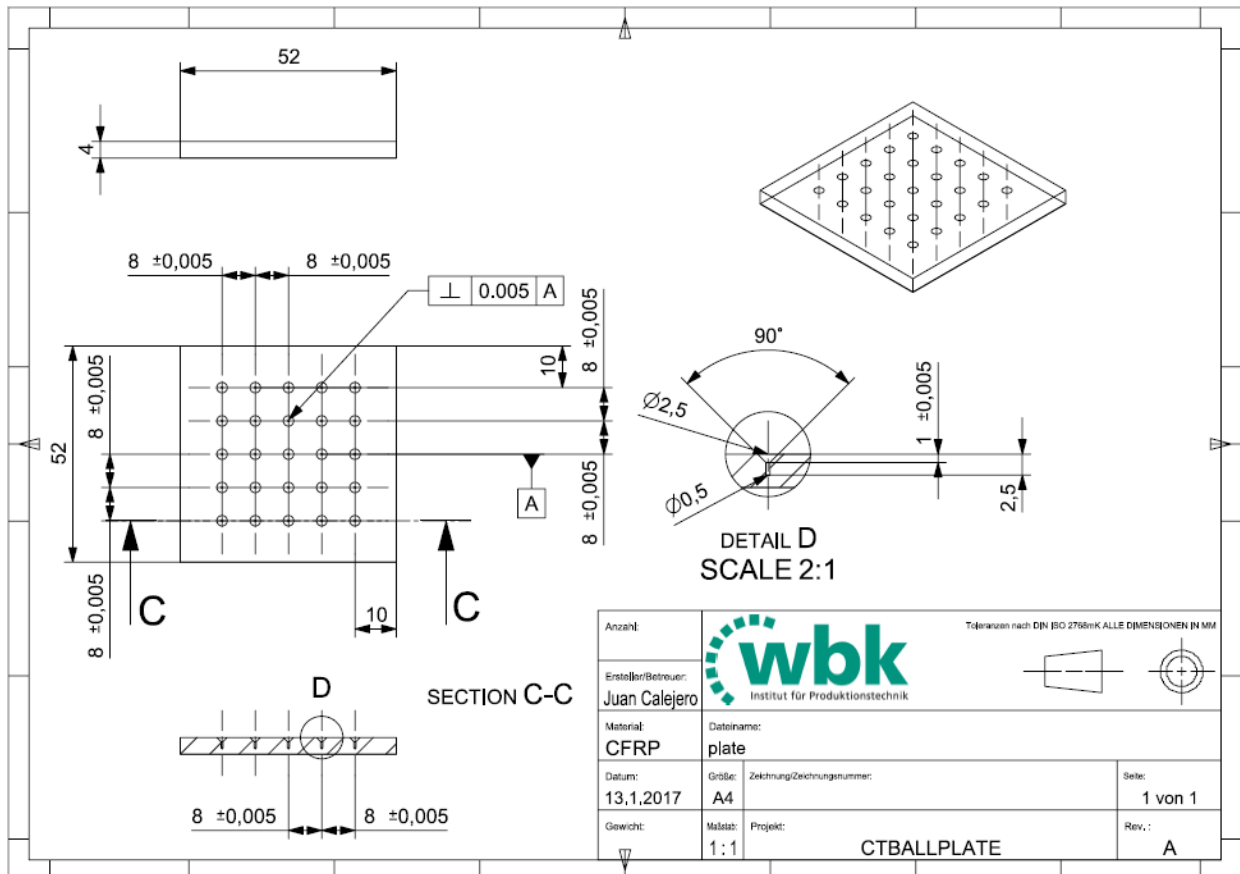


Figure 4-2: CT Ball Plate drawing scheme

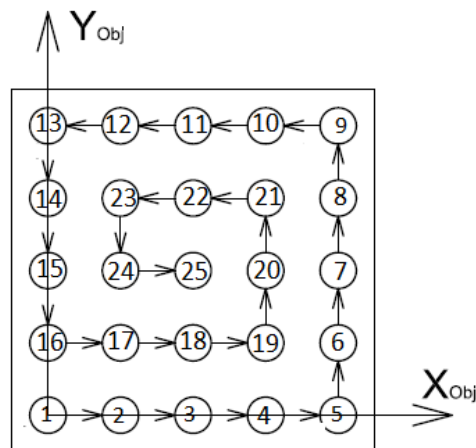


Figure 4-3: CT Ball Plate sphere disposition. Adapted from (Muller P 2012).

As the plate was symmetrical in vertical and horizontal axis, in order to identify the orientation of the CT Ball Plate, a white point was painted in the surface of the CFRP plate, see Figure 4-4.

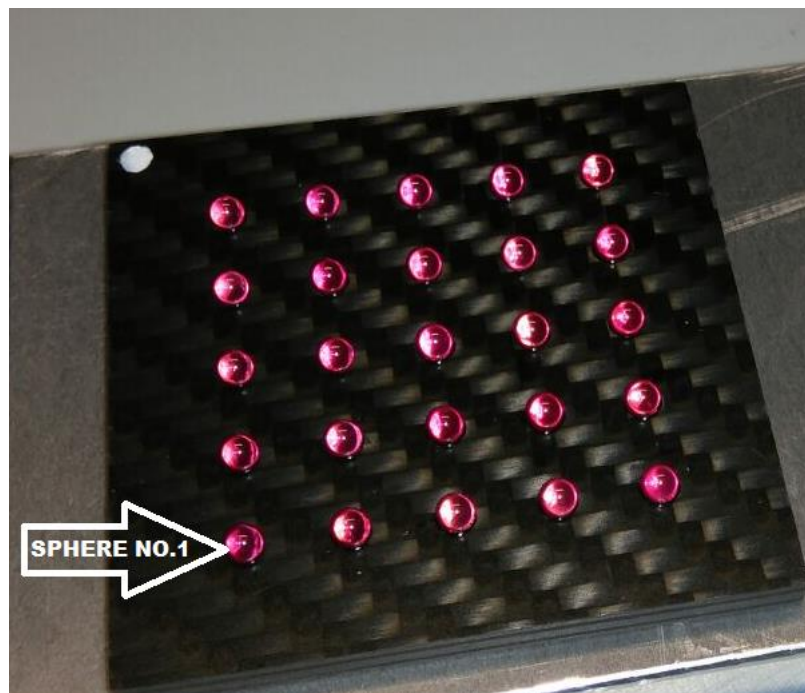


Figure 4-4: CT Ball Plate

4.2 CT Ball Plate calibration in CMM

In order to know precisely the distance between all sphere centers, a calibration in a tactile coordinate measuring machine (CMM) was done. These values from CMM were taken as reference values when comparing them with the values from CT.

The calibration was done in the following steps.

First, it was necessary to calibrate the machine itself. For this purpose, a $\varnothing 25\text{mm}$ Ceramic Sphere was measured three times with a $\varnothing 5\text{mm}$ probe, by comparing those measurands with the supposed measurands of the sphere, the machine calibrated the relative movement between the probe and the platform.

It is interesting to notice that this $\varnothing 5\text{mm}$ probe is only used for calibration procedures, and never for measuring a real object. That way it is more likely to have a more precise calibration procedure, see Figure 4-5.

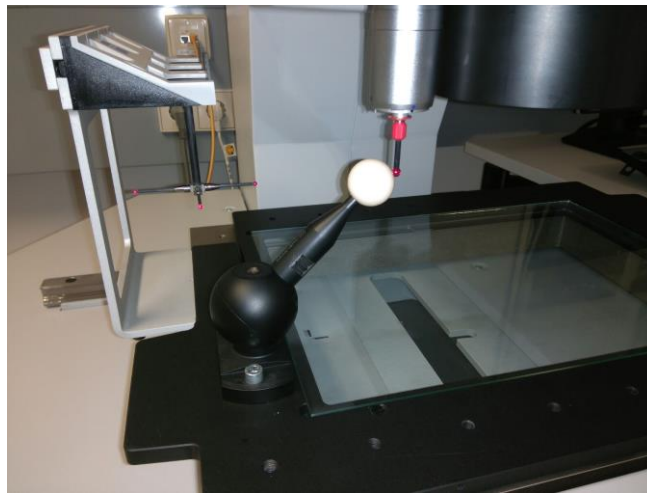


Figure 4-5: Calibration with $\varnothing 5\text{mm}$ probe

Then as the $\varnothing 0,8\text{mm}$ probe was going to be used to measure the CT Ball Plate, it needed also its calibration. The $\varnothing 0,8\text{mm}$ probe measured three times the $\varnothing 25\text{mm}$ Ceramic Sphere, so that the machine could calculate the correction of the radius from $\varnothing 0,8\text{mm}$ probe, when doing the real measurement.

When the machine was fully calibrated, the measurement of the CT Ball Plate started. The measurement was performed two times.

The deviation from nominal values in the first and second measurement is plotted in Figure 4-6 and Figure 4-7. As expected when nominal value is bigger, the value of the deviation increases. The orange line represents how deviation grows when augmenting the nominal value. Deviation is calculated as the distance measured in CMM minus the nominal value.

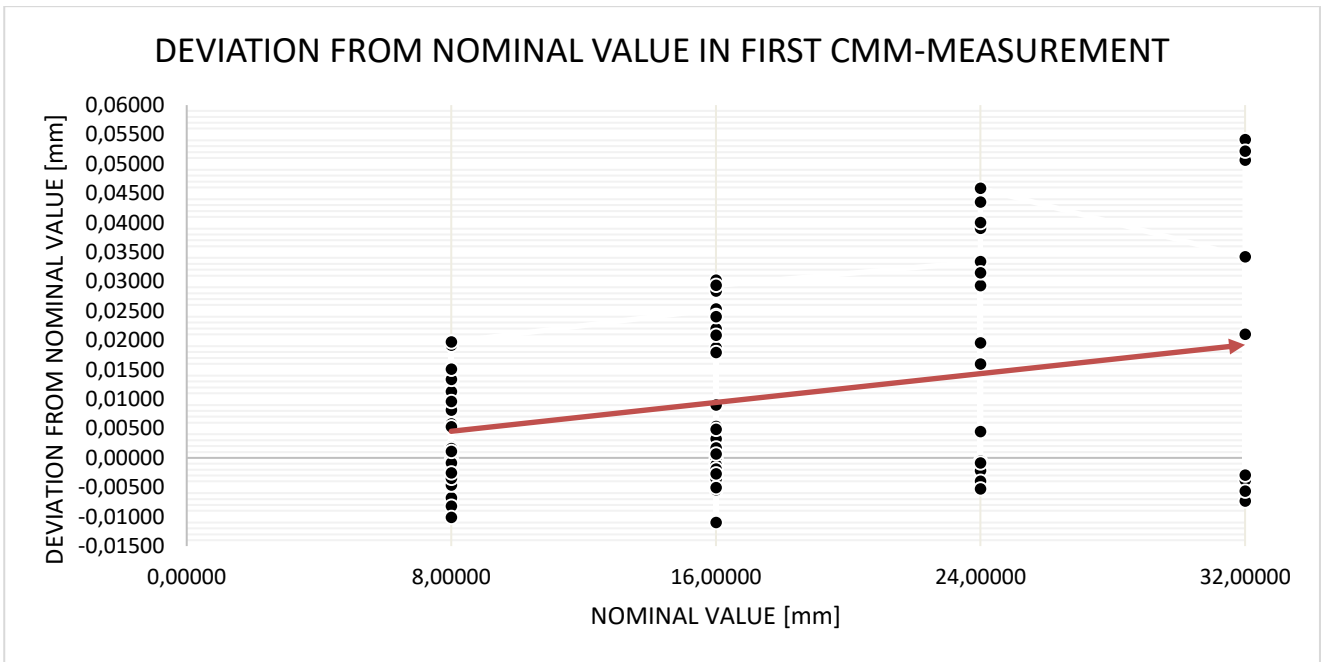


Figure 4-6: Deviation between measurands from first CMM measurement and nominal values

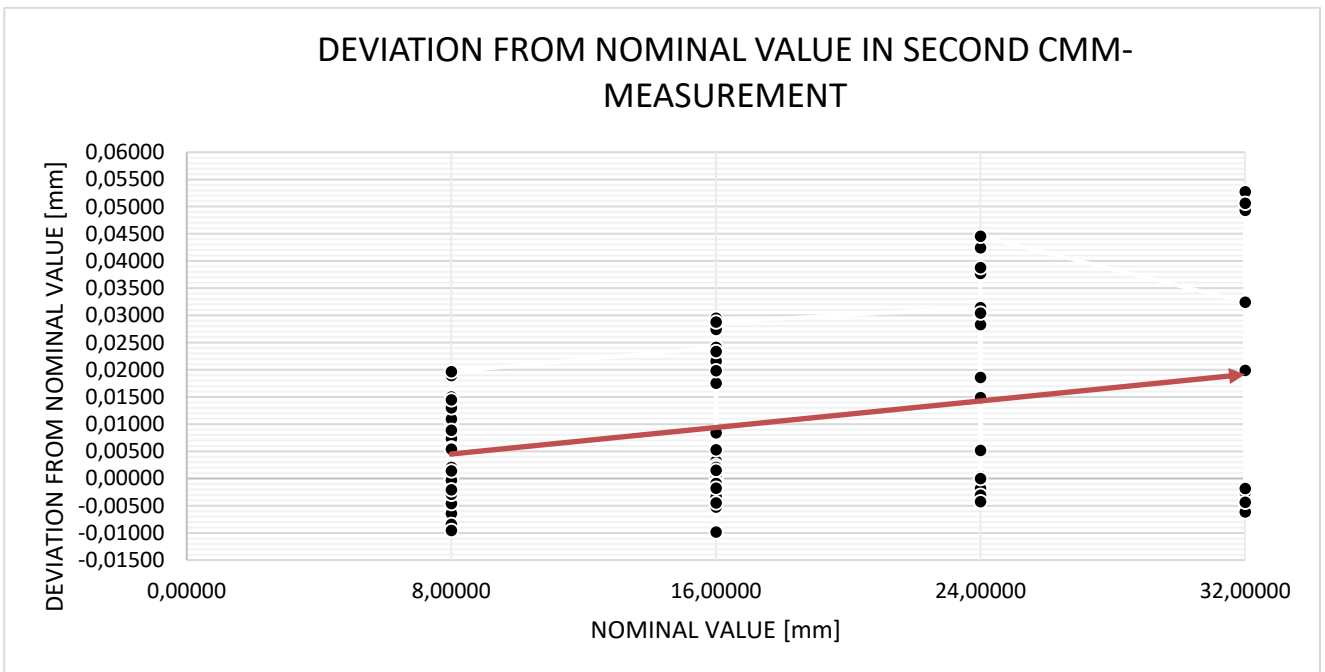


Figure 4-7: Deviation between measurands from second CMM measurement and nominal values

The largest deviation from nominal value in the first measurement was 0,05414mm and the largest deviation from nominal value in the second measurement was 0,05274mm both values corresponded to the 32mm-measurands.

In order to make the study more precise, for the rest of the experiment the average between both CMM measurand values was used. The deviation between both measurands from the first and from the second measurement in CMM is plotted in Figure 4-8. In the worst case the deviation rose up to 0,00194mm.

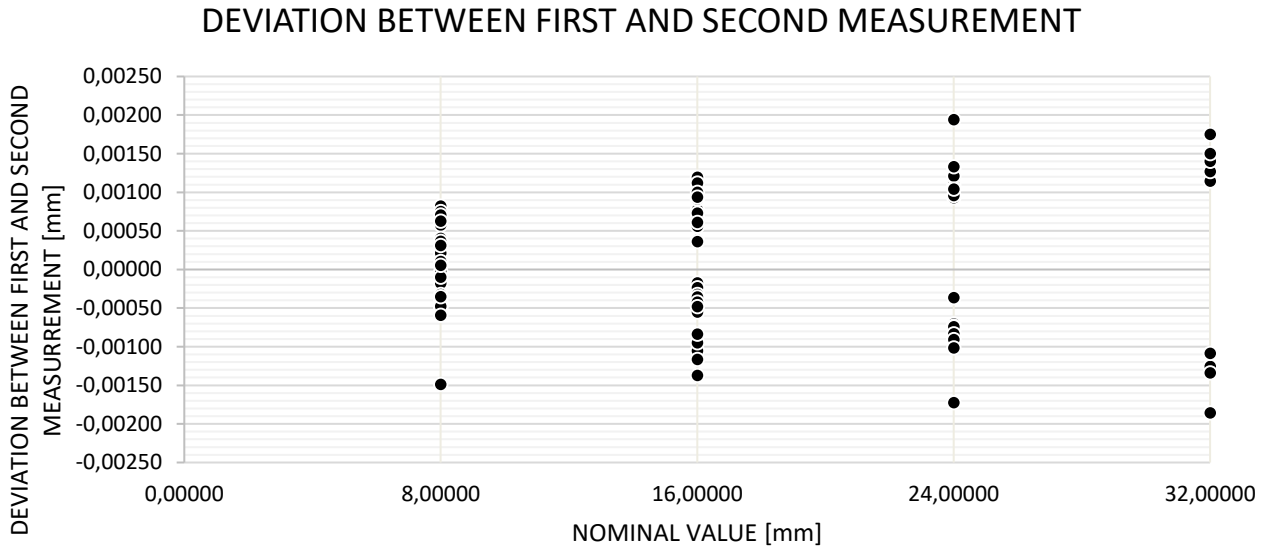


Figure 4-8: Deviation between measurands from first CMM measurement and second CMM measurement in the different nominal values.

4.3 Explanation of the experiments in CT

The experiments were done in a Zeiss Metrotom 800 CT machine. This machine had the following characteristics: a max. voltage of 130kV, a max. intensity of 300 μ A, a power of 39W, minimal focal spot size was 0,005mm and dimensions of planar detector were 1536x1920Px with a pixel size of 127x127 μ m. The distance between source and detector (SDD) was around 800mm.

The CT machine was used to make a complete scan (360°) of the CT Ball Plate. These scans were made at three different magnification positions, or distances between source and object (SOD), those distances were 250mm, 400mm and 550mm from the source in magnification axis. Therefore, measurands with different magnifications were obtained. Magnification value is calculated as appears in Equation 4-1. The value “+15” means that the source was observed to have a small shift from its supposed zero-position.

$$\text{Magnification value} = \frac{(SDD+15)}{(SOD+15)} \quad \text{Equation 4-1}$$

All CT scans were made with 130kV, 105 μ A and they took 1550 pictures in a complete 360° rotation. CT Ball Plate was placed in a way that the centre from projection of sphere no.25 was located approximately in the centre of detector at a vertical height, in Z axis, of about 198,600mm, see Figure 4-9. This position was achieved by manual adjusting of the rotary platform.



Figure 4-9: CT Ball Plate adjusted in clamping

From each CT scan, it was possible to obtain the distances between sphere centres from two different data sources.

One data source was the 3D reconstructed model created by the software of CT. This 3D-model gave a representation of CT Ball Plate which was close to reality but, as the software from CT corrected some errors, it was impossible to base the experiments of this thesis in that data source. Nevertheless, those output data were useful for making a comparison with the data from the next method, in order to estimate its accurateness.

The other data source was based on using the image taken at 270° , actually the image was taken at $270^\circ 13'$, in each of the three scans. The CT provided two different images (both of them with a dimension of 1456×1840 pixels), one original and one corrected.

It is clear to see that in the corrected image has a higher image quality and projections from spheres are more distinguishable, that is why only corrected images were used in the Matlab method, see Figure 4-10.

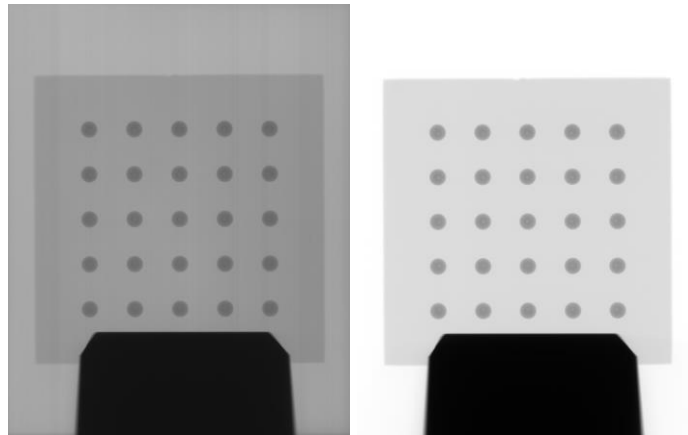


Figure 4-10: (a) Uncorrected image from CT (b) Corrected image from CT

Those images were treated in Matlab to detect the positions of the centres of the projected spheres, see Figure 4-11, 4-12 and 4-13.

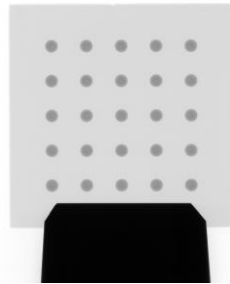


Figure 4-11: Image at a SOD of 250mm.

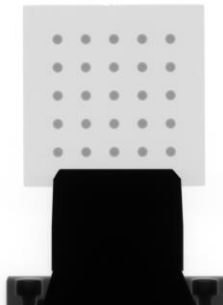


Figure 4-12: Image at a SOD of 400mm.

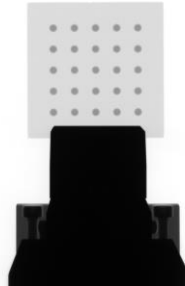


Figure 4-13: Image at a SOD of 550mm.

The Matlab code that was used for this purpose is shown below. The code that appears next was the one used for detecting circles in the image taken at a SOD of 250mm.

```

%%CIRCLES DETECTION PROGRAM
a= imread('X250.tif'); %%it could be another format of image .tif, .jpg,
.jpeg, .gif...
%%For other scans the file would be X400 or X550, for 400mm and 550mm
respectively.
a_cut= a (1:1200, :, :); %%takes a selected part of the image delimiting the region
observed 1:1200px for 250mm, 1:1400px for 400mm and 1:1140px for 550mm.
format long %%in order to show more decimals
figure (1)
imshow (a_cut); %%shows the cut image that it is going to be processed

%%Intern algorithm method
Method='PhaseCode'

Rmin= 35; %%gives a low edge value for the radius of the circles
Rmax= 36; %%gives an upper edge value for the radius of the circles

%%Detection with Sensitivity=1, Sensitivity is a value that enhances the circle
detection by looking for the most evident circular forms in images, experience
tells that Sensitivity should be 1 for 250mm, 0.99 for 400mm and 0.989 for 550mm.

[centers, radii] = imfindcircles(a_cut, [Rmin Rmax], 'ObjectPolarity', 'dark', ...
    'Sensitivity', 1, 'Method', method)
%%Hough transform shows centre positions in two columns first column shows
positions (in pixel) in x-axis and second column shows positions (in pixel) in y-
axis and then the radii of detected circles are shown.

imshow(a) %%shows detected circles in same scan image
h=viscircles (centers, radii, 'EdgeColor', 'b'); %%shows original image with the
detected circles on top of the image circles with a blue edge coloured.
axis equal %%shows the image with a proportion 1:1 of x and y axis

```

It is interesting to remark that it was necessary to cut the image taken from the detector as the clamping was much more distinguishable than the projections of the spheres and that gave problems because the Matlab could not detect any circles out of the images.

For the scan done at a SOD of 250mm, the image was limited between pixel 1 and 1400 in vertical direction, the origin of the pixels was placed in top-left corner of the image.

For the scan done at 400mm the image was limited between pixel 1 and 1200.

Lastly, for the scan done at 550mm the image was limited between pixel 1 and 1140.

Also, the code needed some extra adjustments for each specific scan. For the scan made at 250mm the range of radii used was (35-36) px and a sensitivity of 1, for the scan made at 400mm the range of radii used was (21-22) px and a sensitivity of 0,99 and for the scan made at 550mm the range of radii used was (14-15) px and a sensitivity of 0.989.

With those adjustments implemented, it was possible to achieve a good detection quality. As it was not possible to know which were the exact positions of the centres of those circles, it was likely to think that the more similar the detected radii were with each other for each scan, the closer the centres were to its real value.

Circles detected at a SOD of 250mm, see Figure 4-14, estimated position of the centers from those circles, see Figure 4-15(a) and estimated radii, see Figure 4-15 (b).

Circles detected at a SOD of 400mm, see Figure 4-16, estimated position of the centers from those circles, see Figure 4-17(a) and estimated radii, see Figure 4-17 (b).

Circles detected at a SOD of 550mm, see Figure 4-18, estimated position of the centers from those circles, see Figure 4-19(a) and estimated radii, see Figure 4-19 (b).

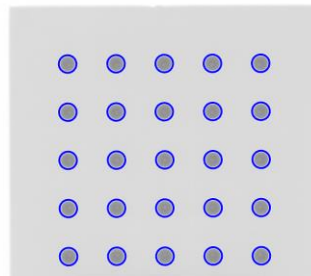


Figure 4-14: Circles detected at 250mm

SPHERE POSITION	POSITION X [px]	POSITION Y [px]	
SPHERE 1	348,45425	1304,43089	35.996089690373779
SPHERE 2	540,49055	1303,40083	35.996376490378687
SPHERE 3	732,57179	1302,00000	35.996320614559053
SPHERE 4	925,00000	1301,50416	35.996219452162514
SPHERE 5	1116,44185	1300,53476	35.996966581735862
SPHERE 6	1115,54941	1108,48305	35.995275658351630
SPHERE 7	1115,48978	916,49018	35.996032958795382
SPHERE 8	1114,55395	725,00000	35.994730470105253
SPHERE 9	1113,56905	533,45094	35.996179471740241
SPHERE 10	921,50535	534,00000	35.996713617502174
SPHERE 11	729,50679	534,49010	35.995884181865492
SPHERE 12	537,48335	535,52032	35.996868554237473
SPHERE 13	345,00000	536,56346	35.996751055524200
SPHERE 14	345,48659	728,46170	35.995649266327469
SPHERE 15	347,00000	920,41825	35.996266688796439
SPHERE 16	347,44962	1112,00000	35.995897237657211
SPHERE 17	539,48401	1111,45717	35.995457958341028
SPHERE 18	732,00000	1110,35815	35.997428922224749
SPHERE 19	924,00000	1109,52447	35.996187233548184
SPHERE 20	923,50764	917,51634	35.996770757279464
SPHERE 21	922,55365	725,58040	35.997180043037176
SPHERE 22	730,00000	726,50989	35.996888777969900
SPHERE 23	537,61059	727,00000	35.996090864275914
SPHERE 24	539,40573	919,42600	35.996492151165043
SPHERE 25	731,51601	918,47363	35.996158008455815

Figure 4-15: (a) Position of the centers of circles at 250mm. (b) Estimated radii at 250mm

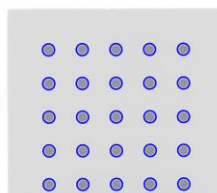


Figure 4-16: Circles detected at 400mm

POSICION DE LAS ESFERAS	POSICION X [px]	POSICION Y [px]	
ESFERA 1	486,95406	1164,45360	21.994424030345556
ESFERA 2	609,56753	1163,58354	21.992705680719073
ESFERA 3	732,46055	1163,49069	21.993846570305742
ESFERA 4	854,58961	1162,51271	21.994591116927328
ESFERA 5	977,44291	1162,46915	21.993611897608517
ESFERA 6	976,53165	1039,53678	21.995258369607559
ESFERA 7	976,57326	917,20836	21.993014755675972
ESFERA 8	976,00000	794,58981	21.994145877933651
ESFERA 9	975,52789	672,52748	21.992864810427751
ESFERA 10	852,52818	673,46578	21.993731229511901
ESFERA 11	730,39700	673,57135	21.993840079191443
ESFERA 12	607,64221	674,40013	21.994327623358238
ESFERA 13	484,79212	674,60247	21.993735532066754
ESFERA 14	485,47437	797,00000	21.995541099438206
ESFERA 15	486,45610	919,53825	21.995528620582448
ESFERA 16	486,55877	1042,03738	21.993442316637037
ESFERA 17	609,45438	1041,50732	21.994545738040710
ESFERA 18	731,96949	1041,00000	21.994745065221039
ESFERA 19	854,44094	1040,47707	21.992803924348316
ESFERA 20	853,72720	917,99754	21.994494480715794
ESFERA 21	853,47101	795,54492	21.992905548240842
ESFERA 22	730,57927	796,00000	21.992905332648604
ESFERA 23	608,00000	796,59610	21.994564799164820
ESFERA 24	608,50814	919,47116	21.994641927279389
ESFERA 25	731,43366	918,49276	21.994509164281215

Figure 4-17: (a) Position of the centers of circles at 400mm. (b) Estimated radii at 400mm

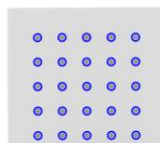


Figure 4-18: Circles detected at 550mm

POSICION DE LAS ESFERAS	POSICION X [px]	POSICION Y [px]	
ESFERA 1	552,43336	1099,25511	14.992699473729061
ESFERA 2	642,43688	1098,58869	14.991624701715217
ESFERA 3	732,09241	1098,48911	14.991507178860910
ESFERA 4	822,45960	1098,41336	14.990734167826174
ESFERA 5	912,02689	1097,72756	14.991778569746327
ESFERA 6	911,54192	1008,00000	14.992044345468450
ESFERA 7	911,57224	917,61311	14.992660742226759
ESFERA 8	910,63137	828,39238	14.992750358580084
ESFERA 9	910,62776	738,16575	14.985102558826158
ESFERA 10	820,55923	738,45702	14.991891726885910
ESFERA 11	730,56964	738,61321	14.992365173640430
ESFERA 12	640,54261	739,13482	14.993513663896678
ESFERA 13	550,53539	739,72061	14.992749848993924
ESFERA 14	550,84365	829,70256	14.989289195659595
ESFERA 15	551,47366	919,45798	14.992102257809316
ESFERA 16	552,05557	1009,15385	14.992102257809316
ESFERA 17	642,00000	1008,59903	14.990498640940828
ESFERA 18	731,56188	1008,43585	14.991195188431162
ESFERA 19	821,68373	1007,77542	14.991332435417105
ESFERA 20	821,48239	918,41811	14.991385191413906
ESFERA 21	821,37296	828,58487	14.991380063122026
ESFERA 22	730,96527	828,50930	14.992041479690217
ESFERA 23	641,13646	829,06676	14.992905510651431
ESFERA 24	641,47427	918,95458	14.992015536256458
ESFERA 25	731,49201	918,55204	14.993101532042896

Figure 4-19: (a) Position of the centers of circles at 550mm. (b) Estimated radii at 550mm

Then, when the centres of the projections were detected, the distance between the different circles was obtained. It should be noted that this distance was in pixel units, so it needed a conversion into micrometers as shown in Equation 4-2.

$$Distance[\mu m] = Distance[px] * 127 \quad \text{Equation 4-2}$$

As the pixel size in the detector was 127x127 micrometers, appeared 127 in the formula.

But this distance was very different in the three different scans, as they had different SODs. Therefore, it was necessary to apply the magnification value to transform the measurands, as shown in Equation 4-3.

$$Real\ Distance[\mu m] = \frac{Magnified\ Distance[\mu m]}{Magnification\ value} \quad \text{Equation 4-3}$$

These real distances were two hundred seventy-nine in total, ninety-three measurands per magnification position.

It is interesting to notice that all the distances when CT Ball Plate was closer to detector were further from their supposed nominal values as those distances measured when CT Ball Plate was closer to source, in other words, distances measured at 250mm were more reliable than those measured at 400mm and specially 550mm. Also, as obvious, when the measurand increased, the deviation produced was bigger, see Figure 4-20, 4-21, 4-22. Deviation was calculated as the difference between measurand by CT and nominal value.

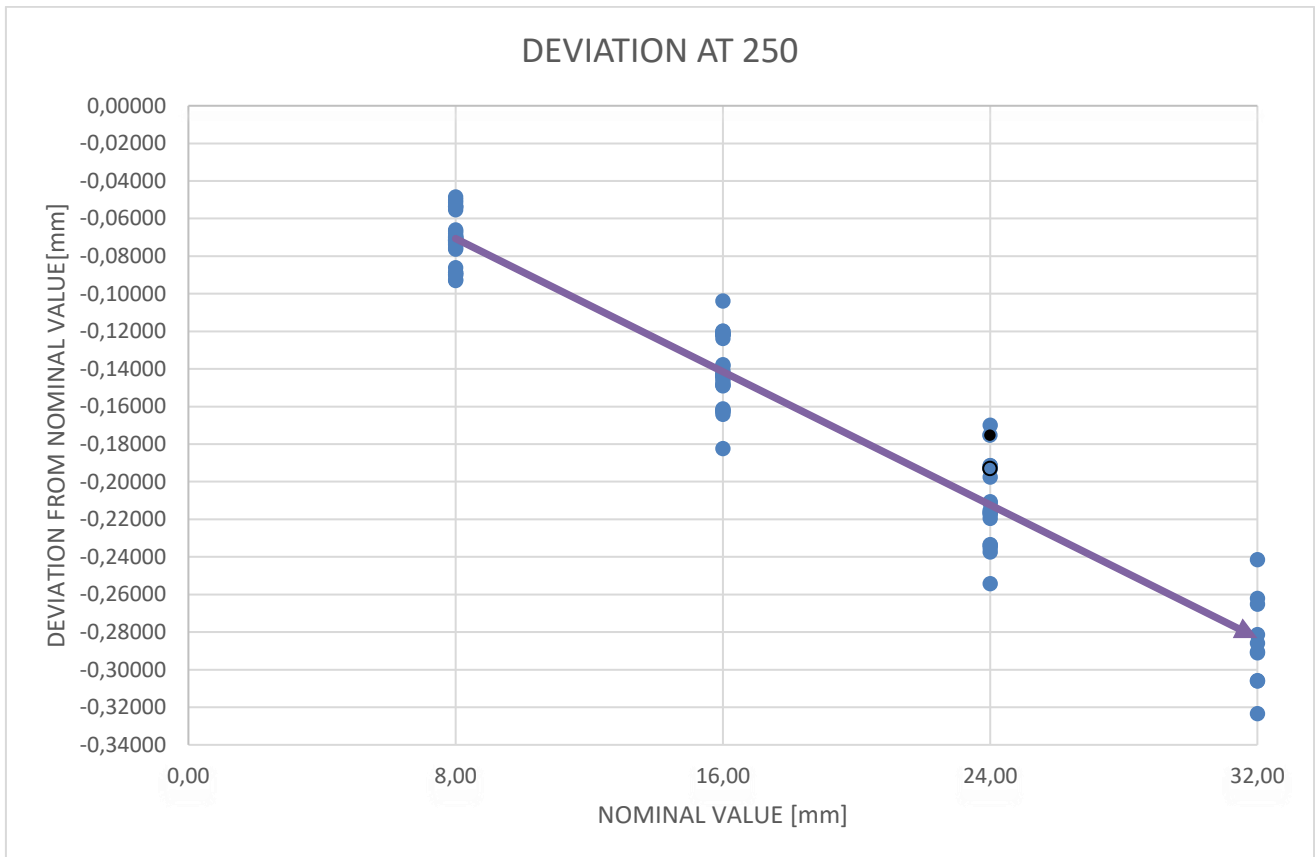


Figure 4-20: Deviation of CT measurands from nominal value at 250mm

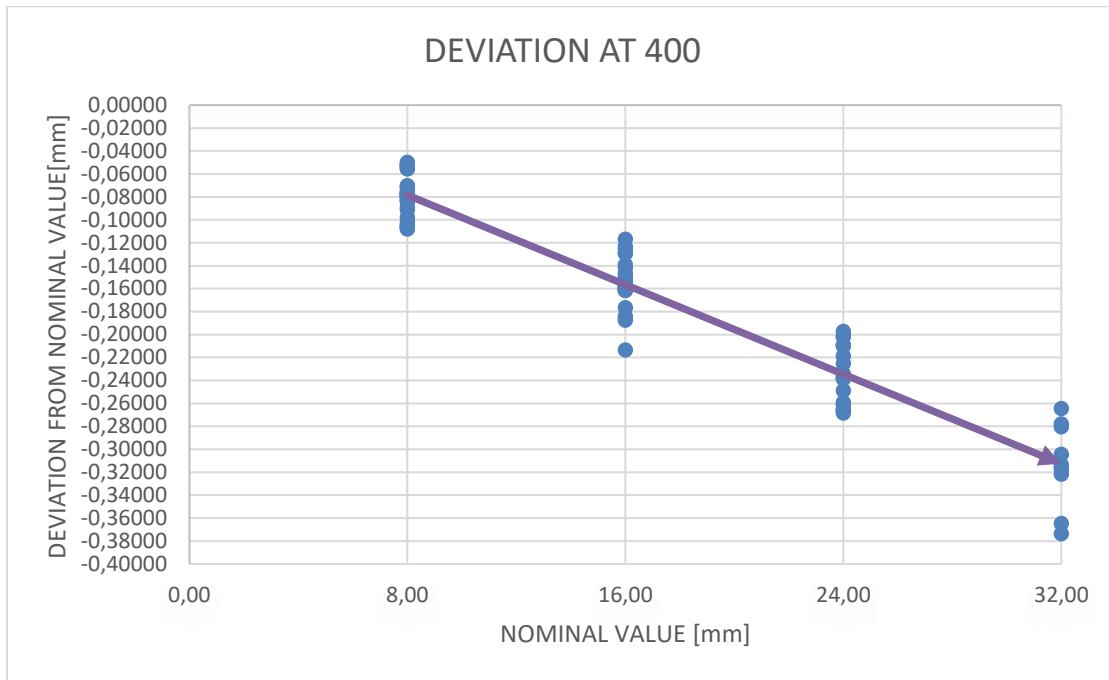
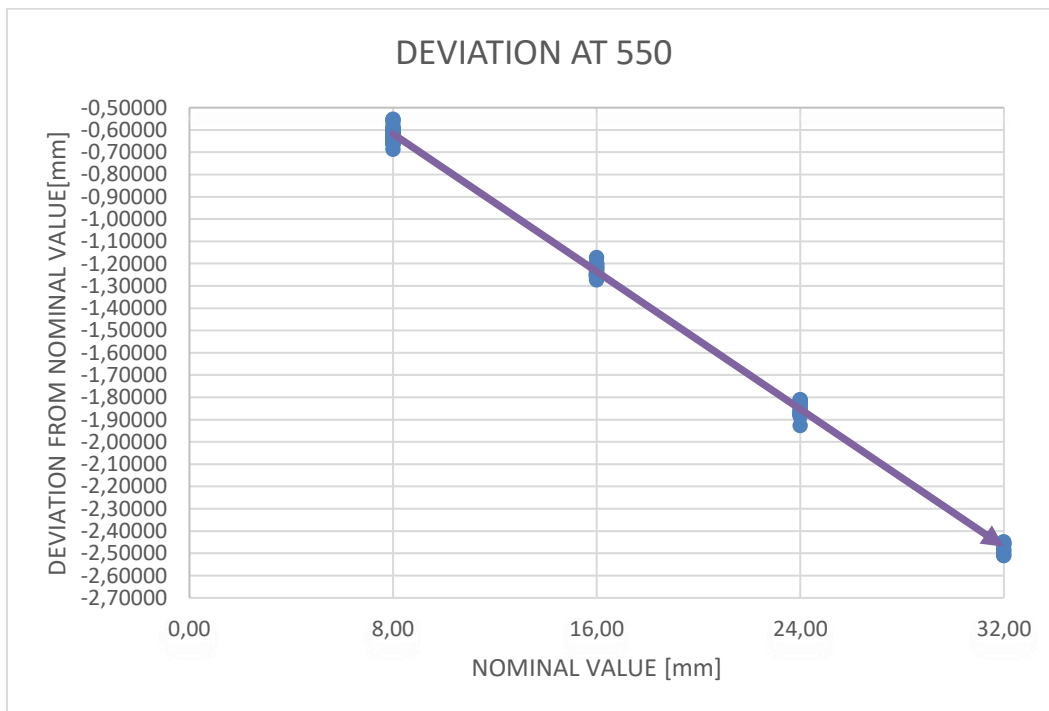


Figure 4-21: Deviation of CT measurands from nominal value at 400mm



Also, it would be interesting to notice the difference between those values of the distances given by Matlab and those values of the distances given by reconstructed 3D model. In the plot, deviation is represented against their nominal value, deviation of the values was calculated as the distance in 3D model minus the distance in Matlab model. Therefore, an estimation of the accurateness of Matlab method could be seen, see Figure 4-23, 4-24 and 4-25. As expected, there were more deviations when nominal value increased and when SOD value increased.

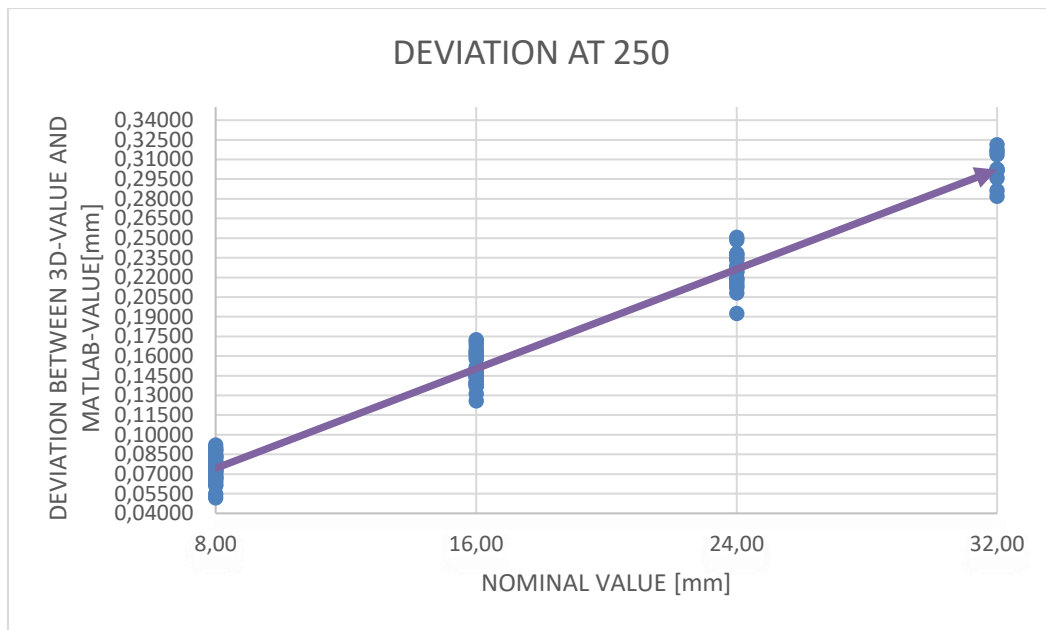


Figure 4-23: Deviation between 3D-model-values and Matlab-values at 250mm against their nominal distances.

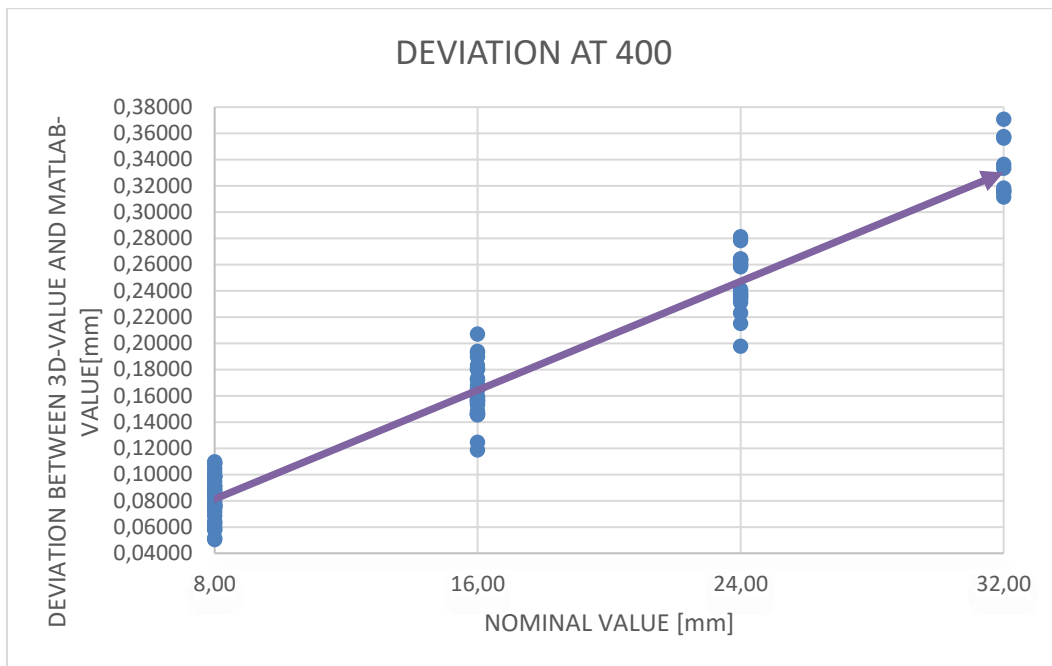


Figure 4-24: Deviation between 3D-model-values and Matlab-values at 400mm against their nominal distances.

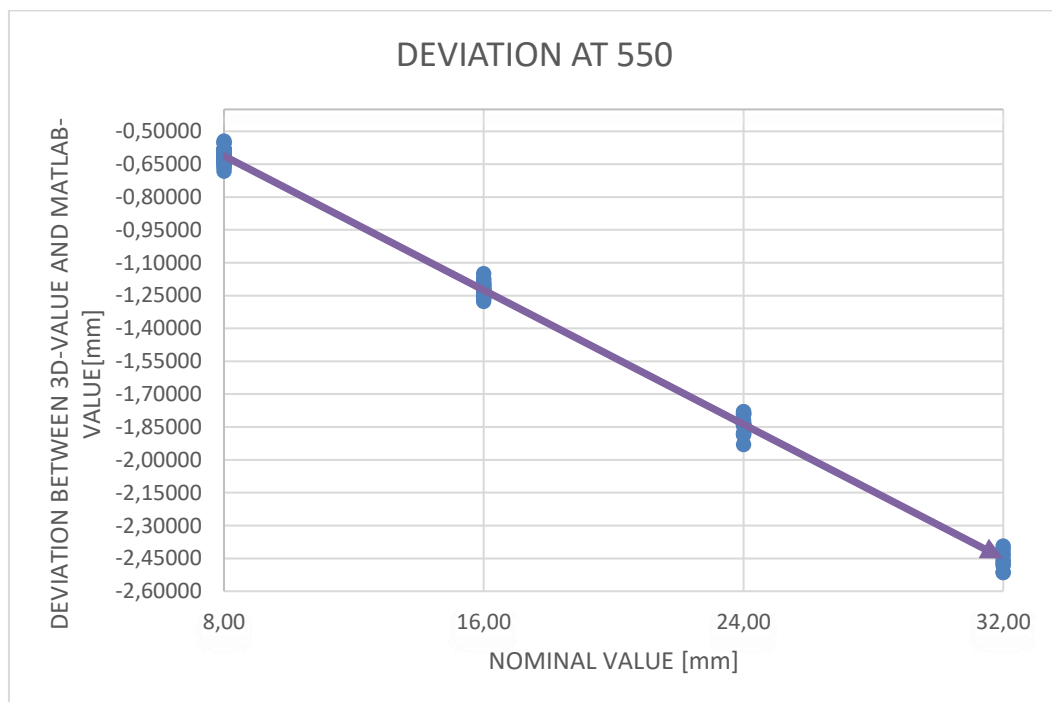


Figure 4-25: Deviation between 3D-model-values and Matlab-values at 550mm against their nominal distances.

These measurands from Matlab method were used in sections 4.3.1 and 4.3.2 to determine scale error and angular misalignments of the detector.

4.3.1 Estimation of angular misalignments of the detector

As mentioned before in section 2.3.1, in a CT if detector is tilted, slanted or skewed, it will give a deformed projection of real object when doing the CT scan, therefore giving “fake” measurands.

The purpose of the following method was to estimate the angular misalignments of the detector, such as tilt, slant or skew. For this method, the distances between the centers of sphere projections, from Matlab method, were needed, but only those contained in the central axes, horizontal and vertical, were used. In order to enhance the accurateness of the method only the distances from the image at a SOD of 250mm were used. As seen in the plots from past section, those distances were closer to nominal value.

To estimate tilt (θ), or rotation of detector about X-axis, see Figure 2-15, the distances between those projections of spheres contained in vertical central axis were used, that means, projections from spheres no.11, 22, 25, 18 and 3, see Figure 4-26. The reason why those projections of spheres were used was because, as they were in the central vertical axis of the detector they were less likely to have been affected by slant deviation.

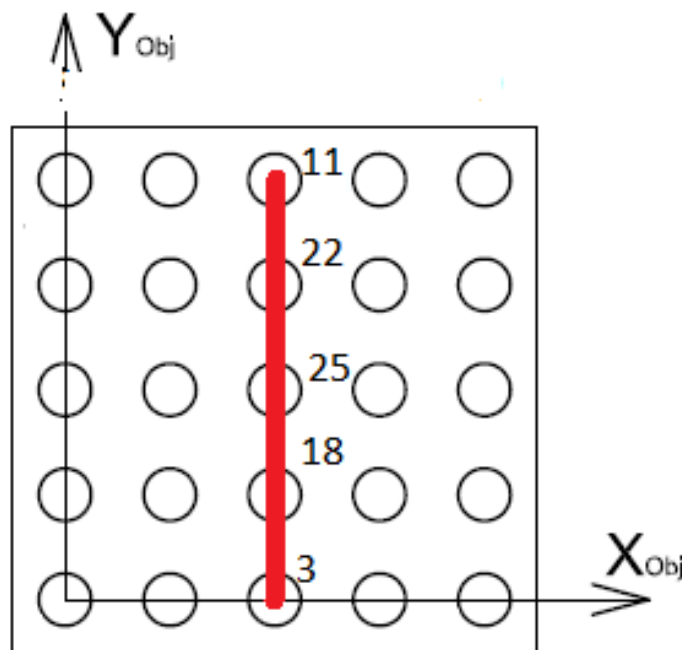


Figure 4-26: Distances used in tilt estimation process. Adapted from (Muller P 2012).

Now, it is clear to see that if detector would have been perpendicular to central ray, tilt would have been 0° . This situation would be referred as the ideal situation. But, as it was likely to have some tilt in the detector, it was necessary to consider the real situation, see Figure 4-27.

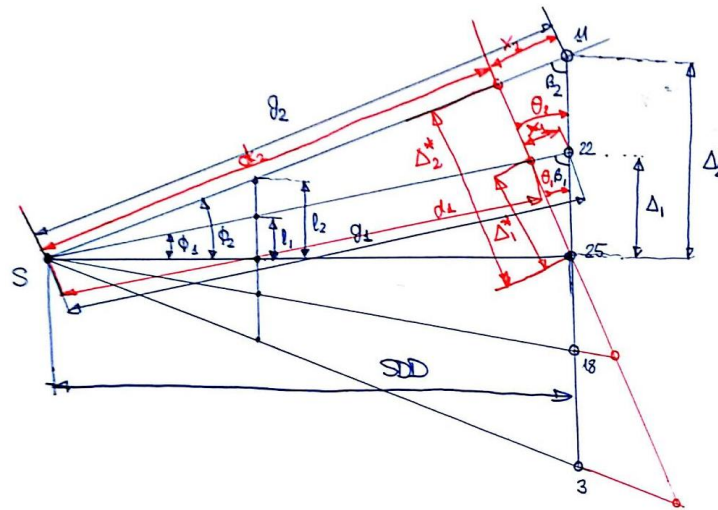


Figure 4-27: Ideal and real situation for tilt estimation process

In the drawing, it is possible to distinguish that red lines correspond to real situation, whereas blue lines correspond to ideal situation.

As the source-to-object distance (SOD), 250mm+15mm, source-to-detector distance (SDD), 800mm+15mm, and the calibrated distance between sphere centers (l_1) at the object, from CMM, were known, the ideal situation could be imagined. Then, value, Δ_1 , which was the ideal distance between the centers of projections of the spheres no.22 and 25 in ideal situation in CT, could be calculated with Equation 4-4. The value obtained from each equation is in red color.

$$\Delta_1 = l_1 * \frac{SDD}{SOD} \quad \text{Equation 4-4}$$

Then the distance between source and ideal position of projection from sphere no.22, g_1 , could be obtained with Equation 4-5.

$$g_1 = \sqrt{\Delta_1^2 + SDD^2} \quad \text{Equation 4-5}$$

Afterwards, the angular amplitude of the ray that pointed the projection of sphere no.22, ϕ_1 , in ideal and in real situation, could be calculated with Equation 4-6.

$$\tan(\phi_1) = \frac{\Delta_1}{SDD} \quad \text{Equation 4-6}$$

Then, by looking at the value of the measurand between the projection of spheres no.22 and 25 that CT offered (obviously in real situation and without applying magnification factor) Δ_1^* , and applying it in Equation 4-7, the distance between source and real position of the projection of sphere no.22, d_1 , could be obtained. Equation 4-7 is an application of cosine theorem.

$$\Delta_1^{*2} = SDD^2 + d_1^2 - 2 * d_1 * SDD * \cos(\Phi_1) \quad \text{Equation 4-7}$$

Next, the distance that projection of sphere no.22 moved from its ideal position, x_1 , could be easily estimated with Equation 4-8.

$$x_1 = g_1 - d_1 \quad \text{Equation 4-8}$$

And finally, the angle of tilt could be estimated with Equation 4-9, also obtained from cosine law:

$$x_1^2 = \Delta_1^{*2} + \Delta_1^2 - 2 * \Delta_1^* * \Delta_1 * \cos(\theta_{22-25}) \quad \text{Equation 4-9}$$

The process with the projections of spheres no.11 and 25 was very similar, see Equations 4-10 to 4-15.

$$\Delta_2 = l_2 * \frac{SDD}{SOD} \quad \text{Equation 4-10}$$

$$g_2 = \sqrt{\Delta_2^2 + SDD^2} \quad \text{Equation 4-11}$$

$$\tan(\Phi_2) = \frac{\Delta_2}{SDD} \quad \text{Equation 4-12}$$

$$\Delta_2^{*2} = SDD^2 + d_2^2 - 2 * d_2 * SDD * \cos(\Phi_2) \quad \text{Equation 4-13}$$

$$x_2 = g_2 - d_2 \quad \text{Equation 4-14}$$

$$x_2^2 = \Delta_2^{*2} + \Delta_2^2 - 2 * \Delta_2^* * \Delta_2 * \cos(\theta_{11-25}) \quad \text{Equation 4-15}$$

For more precision in the method, Equations 4-4~4-9 were applied with the projections from spheres no.18 and no.25 and Equations 4-10~4-15 were applied with the projections from spheres no.3 and no.25.

Then the final tilt value could be calculated just by averaging all tilt angles obtained, as states Equation 4-16.

$$\theta = \frac{\theta_{22-25} + \theta_{11-25} + \theta_{18-25} + \theta_{3-25}}{4} \quad \text{Equation 4-16}$$

To estimate slant (φ), or rotation of detector about Y axis, see Figure 2-18, the distances between the projection of spheres contained in horizontal central axis were used, that means, projections from no.15, 24, 25, 20 and 7, see Figure 4-28. The reason why these projections were used was because as they were in the central horizontal axis of detector they were less likely to have been affected by tilt.

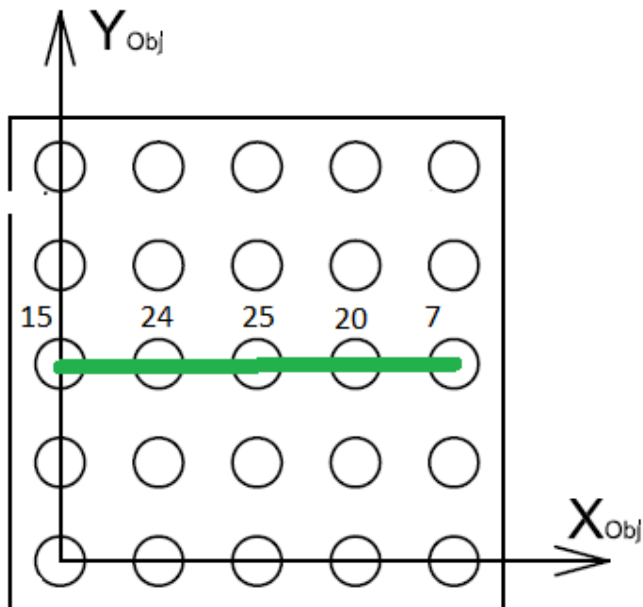


Figure 4-28: Distances used in slant estimation process. Adapted from (Muller P 2012).

Now, it is clear to see that if the detector would have been perpendicular to central ray, slant would have been 0° , then this situation would be referred as the ideal situation. But as it was likely to have some slant in detector, it was necessary to consider the real situation, see Figure 4-29.

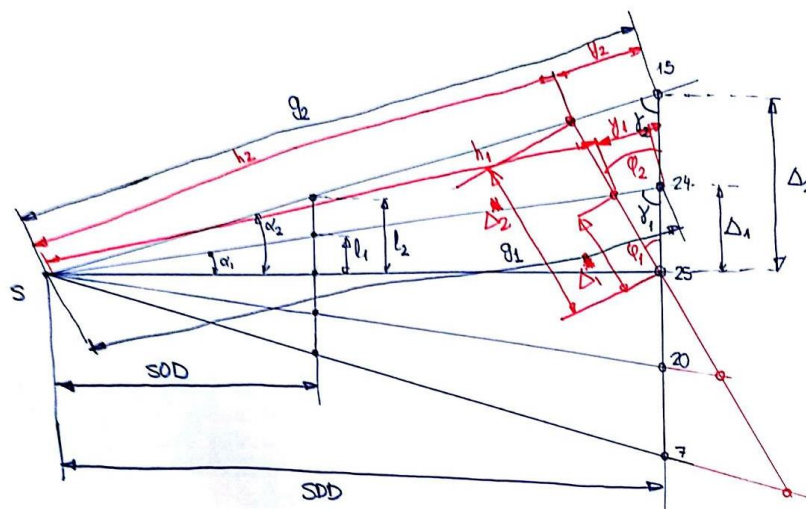


Figure 4-29: Ideal and real situation for slant estimation process

In the drawing, it is possible to distinguish that red lines correspond to real situation, whereas blue lines correspond to ideal situation.

As source-to-object distance (SOD), 250mm+15mm, source-to-detector distance (SDD), 800mm+15mm, and calibrated distance between sphere centers (l_1) at the object, from CMM, were known, ideal situation could be imagined. Then, value Δ_1 , which would be the distance between projections of no.24 and 25 in ideal situation in CT, could be calculated with Equation 4-17.

$$\Delta_1 = l_1 * \frac{SDD}{SOD} \quad \text{Equation 4-17}$$

Then the distance between source and ideal position of the projection from no.24, g_1 , could be obtained with Equation 4-18.

$$g_1 = \sqrt{\Delta_1^2 + SDD^2} \quad \text{Equation 4-18}$$

Afterwards, the angular amplitude of the ray that points the projection of sphere no.24, α_1 , in ideal and in real situation, could be calculated with Equation 4-19.

$$\tan(\alpha_1) = \frac{\Delta_1}{SDD} \quad \text{Equation 4-19}$$

Then, by looking at the value of the measurand between centers of the projections from no.24 and 25 that CT offered, (obviously in the real situation and without applying magnification factor) Δ'_1 , and applying it in Equation 4-20, the distance between source and real position of projection from sphere no.24, h_1 , could be obtained. Equation 4-20 is an application of cosine theorem.

$$\Delta'_1{}^2 = SDD^2 + h_1^2 - 2 * h_1 * SDD * \cos(\alpha_1) \quad \text{Equation 4-20}$$

Next, the distance that projection of sphere no.24 moved from its ideal position, y_1 , could be easily estimated with Equation 4-21.

$$y_1 = g_1 - h_1 \quad \text{Equation 4-21}$$

And finally, the angle of slant could be estimated with Equation 4-22, also obtained from cosine law:

$$y_1^2 = \Delta'_1{}^2 + \Delta_1^2 - 2 * \Delta'_1 * \Delta_1 * \cos(\varphi_{24-25}) \quad \text{Equation 4-22}$$

The process with projections from no.15 and 25 was very similar, see Equations 4-23 to 4-28.

$$\Delta_2 = l_2 * \frac{SDD}{SOD} \quad \text{Equation 4-23}$$

$$g_2 = \sqrt{\Delta_2^2 + SDD^2} \quad \text{Equation 4-24}$$

$$\tan(\alpha_2) = \frac{\Delta_2}{SDD} \quad \text{Equation 4-25}$$

$$\Delta_2'^2 = SDD^2 + h_2^2 - 2 * h_2 * SDD * \cos(\alpha_2) \quad \text{Equation 4-26}$$

$$y_2 = g_2 - h_2 \quad \text{Equation 4-27}$$

$$y_2^2 = \Delta_2'^2 + \Delta_2^2 - 2 * \Delta_2' * \Delta_2 * \cos(\varphi_{15-25}) \quad \text{Equation 4-28}$$

For more precision in the method, Equations 4-17~4-22 were applied with the projections from spheres no.20 and no.25 and Equations 4-23~4-28 were applied with the projections from spheres no.7 and no.25.

Then the final slant value could be calculated just by averaging all slant angles obtained, as states Equation 4-29.

$$\varphi = \frac{\varphi_{24-25} + \varphi_{15-25} + \varphi_{20-25} + \varphi_{7-25}}{4} \quad \text{Equation 4-29}$$

To estimate the skew value, it was necessary to use a different method as with tilt and slant. As when affected by skew, all projections were skewed the same amount of degrees then it was irrelevant if they were on the central horizontal axis or in the central vertical axis.

For example, the estimation was done with central vertical axis as appears in Figure 4-4. Therefore, as in the other cases, there was an ideal and a real scenario, as shown in Figure 4-30.

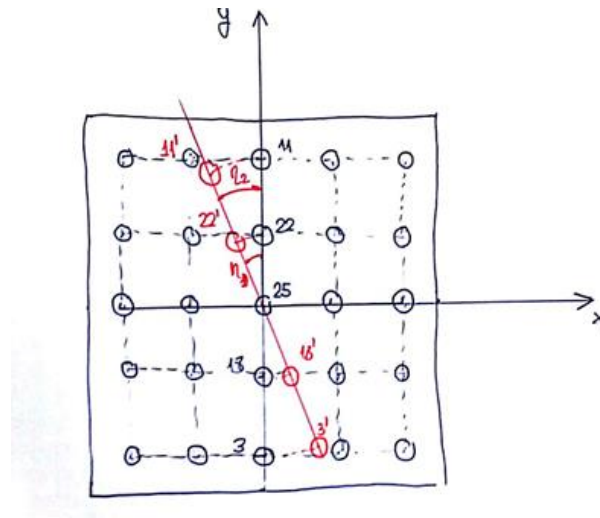


Figure 4-30: Ideal and real situation for skew estimation process

In the drawing, it is possible to distinguish that the red lines correspond to the real situation, whereas the blue lines correspond to the ideal situation

By using the X and Y coordinates of the centre of the projections of sphere no.22 and no.11 it was possible to obtain the skew angles with Equation 4-30 and 4-31.

$$\eta_{22-25} = \arctan\left(\frac{X_{22}-X_{25}}{Y_{22}-Y_{25}}\right) \quad \text{Equation 4-30}$$

$$\eta_{11-25} = \arctan\left(\frac{X_{11}-X_{25}}{Y_{11}-Y_{25}}\right) \quad \text{Equation 4-31}$$

For more precision in the method Equation 4-30 was applied with the projections from spheres no.18 and no.25 and Equations 4-31 was applied with the projections from spheres no.3 and no.25.

Then the final skew value could be calculated just by averaging all skew angles obtained, as states Equation 4-32.

$$\eta = \frac{\eta_{22-25} + \eta_{11-25} + \eta_{18-25} + \eta_{3-25}}{4} \quad \text{Equation 4-32}$$

Once the three methods to obtain tilt, slant and skew are explained. The input values that were used for calculations are exposed, see Table 4-1, 4-2, 4-3.

Table 4-1: Input values for tilt estimation method

$\theta [^\circ]$	l_1 [mm]	l_2 [mm]	Δ_1^* [mm]	Δ_2^* [mm]
θ_{22-25}	8,00534	-	24,38015	-
θ_{11-25}	-	15,99777	-	48,76658

θ_{18-25}	8,00180	-	24,36941	-
θ_{3-25}	-	15,99906	-	48,70803

Table 4-2: Input values for slant estimation method

$\varphi [^\circ]$	l_1 [mm]	l_2 [mm]	Δ'_1 [mm]	Δ'_2 [mm]
φ_{24-25}	8,01111	-	24,39831	-
φ_{15-25}	-	16,02176	-	48,83416
φ_{20-25}	8,00925	-	24,38324	-
φ_{7-25}	-	16,02830	-	48,76532

Table 4-3: Input values for skew estimation method

η	X_{11}	Y_{11}	X_{22}	Y_{22}	X_{25}	Y_{25}	X_{18}	Y_{18}	X_3	Y_3
η_{22-25}	-	-	730,00000	726,50989	731,51601	918,47363	-	-	-	-
η_{11-25}	729,50679	534,49010	-	-	731,51601	918,47363	-	-	-	-
η_{18-25}	-	-	-	-	731,51601	918,47363	732,00000	1110,35815	-	-
η_{3-25}	-	-	-	-	731,51601	918,47363	-	-	732,57179	1302,00000

4.3.2 Estimation of scale error

As mentioned before the other source of error that was considered in this thesis was the focal spot movement, see section 2.3.2, which is another important factor to take into account when studying geometrical error in CT machines.

The method that was used here, was based in the method developed at DTU for scale error determination, see section 3.1.

When the CMM calibration measurement of the CT Ball Plate had been done, the distances between sphere centres were known with high accuracy. Then a comparison between those distances given by CMM and measurands obtained by CT scan was needed. This comparison was done with a linear regression, in order to be able to correct the measurands from objects in future.

The correlation displayed a mathematical formula to calculate the Sphere Distance Error (SDE), expressed by Equation 4-33, when having a calibrated measurand, see Equation 4-34.

$$SDE = L_{CT} - L_{CMM} \quad \text{Equation 4-33}$$

$$SDE = L_{CMM} * a + b \quad \text{Equation 4-34}$$

To obtain the real Equation 4-34, all the distances between sphere centres in CMM and between projection centres in CT were plotted, so as to have in an Excel graphic the calibrated length from CMM in X-axis and the SDE in Y-axis.

5 Results

5.1 Results from estimation of angular misalignments of the detector

The methods from section 4.3.1. were applied and these were the results of tilt, see Table 5-1:

Table 5-1: Estimated tilt values

θ_{22-25}	1,64076°
θ_{11-25}	3,43107°
θ_{18-25}	1,64469°
θ_{3-25}	3,42192°

From Equation 4-16, the final tilt value obtained was $\theta = 2,53461^\circ$. As the values from the spheres no.22-no.25 and no.11-no.25 were very different, it was likely to think that the tilt value should have been around the smallest values, 1,64°. The reason for this big deviation could be due to inaccuracy of the Matlab method when the distance augments, see Figure 4-20.

The methods from section 4.3.1. were applied and these were the results of slant, see Table 5-2:

Table 5-2: Estimated slant values.

φ_{24-25}	1,64727°
φ_{15-25}	3,43553°
φ_{20-25}	1,63951°
φ_{7-25}	3,42297°

From Equation 4-29, the final slant value obtained was $\varphi = 2,53632^\circ$. As the values from the spheres no.24-no.25 and no.15-no.25 were very different, it was likely to think that the slant value should have been around the smallest values, 1,64°. The reason for this big deviation could be due to inaccuracy of the Matlab method when the distance augments, see Figure 4-20.

The methods from section 4.3.1. were applied and these were the results for the skew, see Table 5-3:

Table 5-3: Estimated skew values.

η_{22-25}	0,45248°
η_{11-25}	0,29980°
η_{18-25}	0,14452°
η_{3-25}	0,15772°

From Equation 4-32, the final skew value obtained was $\eta = 0,26363^\circ$. It is necessary to remark that the CT Ball Plate was placed manually in the clamping, without the help of any gadget for

controlling that the CT Ball Plate was perfectly placed without any skew. So, the value of 0,26363° could derive from there as it is likely to think that there could be no actual skew in detector.

5.2 Results from estimation of scale error

As a result, from the Excel values a linear relation between the calibrated length taken as a reference and the SDE mentioned in section 4.3.2 was obtained. Therefore, it was possible to think that this error was produced by focal spot movement in its majority, because the measurands from the CT Ball Plate were not affected by threshold, as they were between sphere centres, and the images used in the Matlab method were corrected by the CT software reducing sources of non-geometrical error, see Figure 5-1.

This linear relation could be applied in posterior measurands of future objects to correct the geometrical error produced by CT, see Equation 5-1.

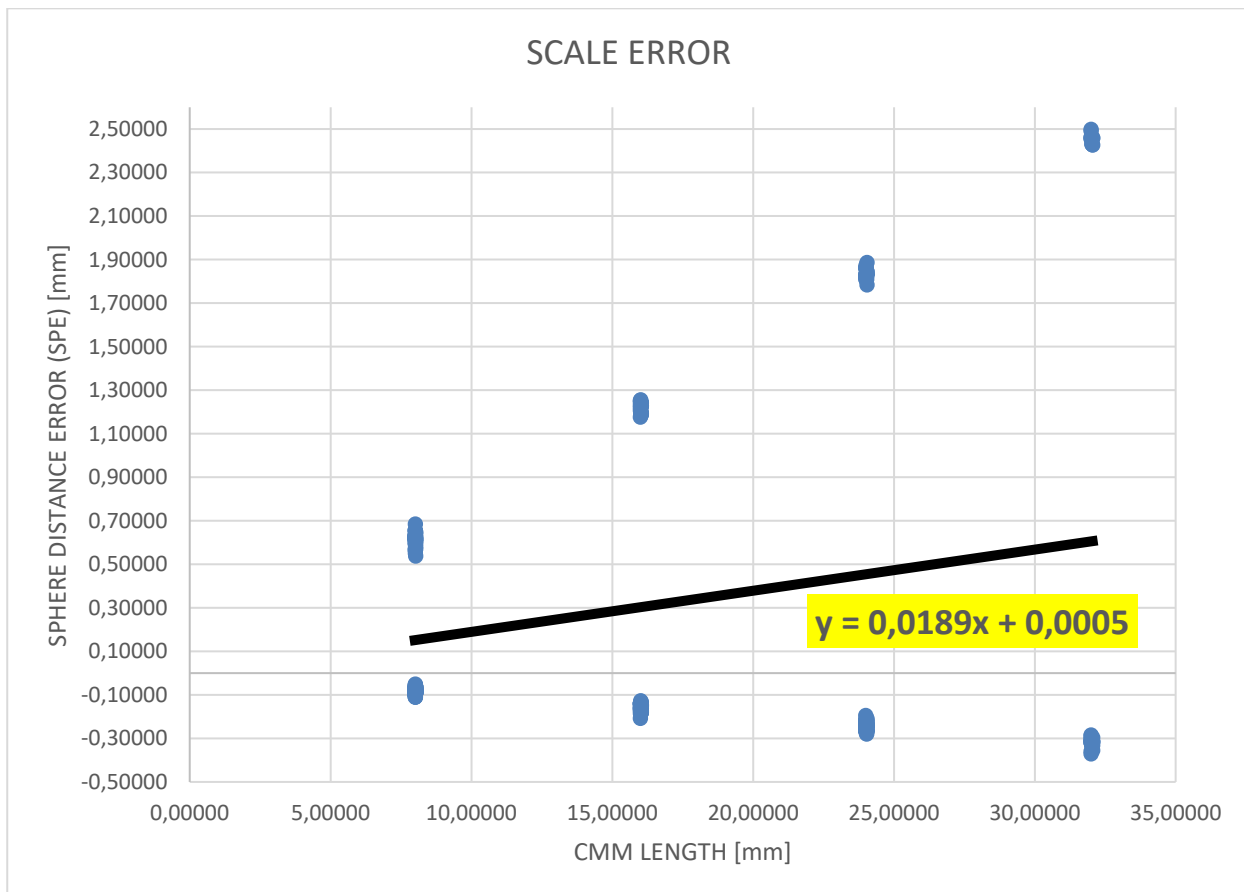


Figure 5-1: Linear relation between CMM and SPE.

$$SPE[mm] = 0,0189 * Calibrated Length [mm] + 0,0005$$

Equation 5-1

The plot includes all the values from the CMM, ninety-three values, and all the values from the CT at the three different magnification positions, two hundred seventy-nine values. It is possible to

see in this distribution that there were lower errors when the distance measured was smaller and when the CT Ball Plate was closer to the source.

6 Discussion

The final results of this thesis were: a linear relation between, the calibrated distance that is measured and the scale error produced by CT when measuring that distance, and the angular misalignments of detector.

Tilt and slant misalignments were a bit bigger as it was thought at first; these deviations could be produced due to an inaccuracy of the Matlab method when providing the final result of the measurands between sphere centres. It is unlikely to think that the detector is tilted and slanted around $1,64^\circ$.

In terms of skew value, the deviation obtained could be produced as a result of the manual fix of CT Ball Plate in clamping, but, as the skew did not present a very large value, it could also be produced due to a real skew in detector.

In terms of the scale error, it is easy to see how big could get the deviation of a measurand from its real value just by applying the linear relation, see Equation 5-1. It is likely to think that those deviations were created mostly due to focal spot movement effect, as others sources of error like threshold do not affect when measuring distances between sphere centres, and the images used in Matlab method were corrected by the software of CT providing images free from non-geometrical sources of error and therefore improving the accuracy of measurands.

7 Summary and Outlook

7.1 Summary

This thesis can be thought as a consecutive piece of work from other thesis developed before, as it treats only the case of the geometrical error. It would only be a small part from the wide range of concepts that CT contains.

In this thesis, the geometrical error was investigated in terms of angular misalignments of the detector and focal spot movement and its effects in scale error.

The experiments were done by taking images at different magnification positions and treat them in Matlab to examine the distances between sphere centers of a reference object, the CT Ball Plate. Those distances were used to estimate some angular misalignments of detector by trigonometrical procedures and to estimate the scale error produced by comparing them with the measurands from a CMM, taken as reference values.

As results, a linear relation of the scale error produced when measuring a certain distance and the quantification of those angular misalignments were obtained.

7.2 Outlook

It would be necessary to improve the precision of the methods used in this thesis in the future so as to determine with more accurateness the geometrical errors produced in CT in terms of quantity, effect and correction procedures.

First, it would be necessary to test more measurements, so as to gather different results and then averaging more possible values. All measurements were done only two times in CMM and only one time in CT and also regarding the CT measurements it would also be interesting to test more than three different magnifications positions.

Second, as seen before in the plots from section 4.3, the measurands obtained from Matlab method did not have a high accurateness, so it is likely to think that Matlab is not the most proper tool for this purpose. It would be interesting to test different programs to detect circles in images and then calculating the measurands between sphere centres or even use another way to detect the circles in Matlab. The biggest issue was that, it was impossible to know which were the ideal positions of the centres of projections, leaving in uncertainty if they were deviated due to the CT machine itself or due to Matlab issues.

List of Figures

Figure 2-1: Typical X-ray source. (J.P. Kruth, M. Bartscher, S. Carmignato, R. Schmitt, L. De Chiffre, A. Weckenmann, 2011).	3
Figure 2-2: Radiation spectra. (J.P. Kruth, M. Bartscher, S. Carmignato, R. Schmitt, L. De Chiffre, A. Weckenmann, 2011).	4
Figure 2-3: Influence of source current. (J.P. Kruth, M. Bartscher, S. Carmignato, R. Schmitt, L. De Chiffre, A. Weckenmann, 2011).	5
Figure 2-4: Influence of source voltage. (J.P. Kruth, M. Bartscher, S. Carmignato, R. Schmitt, L. De Chiffre, A. Weckenmann, 2011).	5
Figure 2-5: Factors affecting size and relative position of X-ray spectrum. (Muller P, 2012).	6
Figure 2-6. (Pavel Müller, 2011).	6
Figure 2-7: Emitted and transmitted photons dependence. (Muller P, 2012).	7
Figure 2-8: 2D flat panel detector with cone beam and 1D line detector with fan beam. A grey value profile along one pixel line is shown. (J.P. Kruth, M. Bartscher, S. Carmignato, R. Schmitt, L. De Chiffre, A. Weckenmann, 2011).	8
Figure 2-9: Image magnification and blurring. (J.P. Kruth, M. Bartscher, S. Carmignato, R. Schmitt, L. De Chiffre, A. Weckenmann, 2011).	9
Figure 2-10: More angular poses improve reconstruction accuracy, but enlarge measurement time. (J.P. Kruth, M. Bartscher, S. Carmignato, R. Schmitt, L. De Chiffre, A. Weckenmann, 2011).	10
Figure 2-11: Scheme of CT influence factors from DTU. (Pavel Müller, 2011).	12
Figure 2-12: Mono- and polychromatic radiation curves. (Muller P, 2012).	13
Figure 2-13: Energy-dependent linear attenuation coefficients. (Jochen Hiller, Peter Hornberger, 2016).	14
Figure 2-14: The ideal geometry of a CT system. (Valentina Aloisi, Simone Carmignato, Joseph Schlecht, Eric Ferley, 2017).	16
Figure 2-15: Potential detector angular misalignments including tilt θ (left), slant φ (middle), and skew η (right). Positive rotations are illustrated. (Massimiliano Ferrucci, Richard K Leach, Claudiu Giusca, Simone Carmignato and Wim Dewulf, 2015).	17
Figure 2-16: Ball from study, (Kumar J, Attridge A, Wood P K C and Williams M A, 2011).	17
Figure 2-17: The error in measuring a 2-mm ball bar at various positions and orientations is plotted as a function of detector (a) in-plane rotation, (b) tilt, and (c) slant. (Massimiliano Ferrucci, Richard K Leach, Claudiu Giusca, Simone Carmignato and Wim Dewulf, 2015).	18
Figure 2-18: Object from study, (Wenig P and Kasperl S, 2006).	18
Figure 2-19: Drift in the (x,y) centre coordinates in cold scan. (Nadia FLAY, Wenjuan SUN, Stephen BROWN, Richard LEACH, Thomas BLUMENSATH, 2015).	20
Figure 2-20: The drift in the (x,y) centre coordinates in hot scan. (Nadia FLAY, Wenjuan SUN, Stephen BROWN, Richard LEACH, Thomas BLUMENSATH, 2015)	20
Figure 2-21: Classification of sources of uncertainty. (Nick Van Gestel, 2011).	21

Figure 3-1: The methods to determine geometrical influence factors are separated into two categories: Methods based on the use of reference objects (also known as imaging methods) and the methods based on the use of reference instruments. (Massimiliano Ferrucci, Richard K Leach, Claudiu Giusca, Simone Carmignato and Wim Dewulf, 2015).	24
Figure 3-2: Ball Plate from DTU, (Muller P, 2012).	25
Figure 3-3: Plot. (Muller P, 2012).	25
Figure 3-4: Phantom. (Jintao Zhao, Xiaodong Hu, Jing Zou and Xiaotang Hu, 2015)	26
Figure 3-5. (Jintao Zhao, Xiaodong Hu, Jing Zou and Xiaotang Hu, 2015).	28
Figure 3-6: Tilted detector about the X axis. (Valentina Aloisi, Simone Carmignato, Joseph Schlecht, Eric Ferley, 2017).	29
Figure 3-7: Sphere distance errors for all the six nominal lengths of the ball bar. (Valentina Aloisi, Simone Carmignato, Joseph Schlecht, Eric Ferley, 2017).	30
Figure 3.8: Diameter errors for the seven spheres of the ball bar. (Valentina Aloisi, Simone Carmignato, Joseph Schlecht, Eric Ferley, 2017).	31
Figure 3-9: (a) CT Ball Tree, (b) Invar 27 Sphere gauge. (Müller, Pavel, 2010).	32
Figure 3-10: (a) Calotte Plate and (b) Hole Bar. (Müller, Pavel, 2010).	32
Figure 3-11: (a) Hollow cylinders and (b) Fibre gauge. (Müller, Pavel, 2010).	33
Figure 3-12: (a) Step cylinders with central hole and (b) without central hole. (Müller, Pavel, 2010).	33
Figure 3-13: Pan flute gauge. (Müller, Pavel, 2010).	33
Figure 3-14: Step wedge. (Müller, Pavel, 2010).	34
Figure 4-1: DIN 5401. (Reiff GmbH).	35
Figure 4-2: CT Ball Plate drawing scheme.	36
Figure 4-3: CT Ball Plate sphere disposition. Adapted from (Muller P, 2012).	37
Figure 4-4: CT Ball Plate.	37
Figure 4-5: Calibration with 5mm-diameter probe.	38
Figure 4-6: Deviation between measurands from first CMM measurement and nominal values.	39
Figure 4-7: Deviation between measurands from second CMM measurement and nominal values.	39
Figure 4-8: Deviation between measurands from first CMM measurement and second CMM measurement in the different nominal values.	40
Figure 4-9: CT Ball Plate adjusted in clamping.	41
Figure 4-10: (a) Uncorrected image from CT (b) Corrected image from CT.	42
Figure 4-11: Image at a SOD of 250mm.	42
Figure 4-12: Image at a SOD of 400mm.	42
Figure 4-13: Image at a SOD of 550mm.	43
Figure 4-14: Circles detected at 250mm.	44

Figure 4-15: (a) Position of the centers of circles at 250mm. (b) Estimated radii at 250mm.	45
Figure 4-16: Circles detected at 400mm.	45
Figure 4-17: (a) Position of the centers of circles at 400mm. (b) Estimated radii at 400mm.	46
Figure 4-18: Circles detected at 550mm.	46
Figure 4-19: (a) Position of the centers of circles at 550mm. (b) Estimated radii at 550mm.	47
Figure 4-20: Deviation of CT measurands from nominal value at 250mm.	48
Figure 4-21: Deviation of CT measurands from nominal value at 400mm.	49
Figure 4-22: Deviation of CT measurands from nominal value at 550mm.	49
Figure 4-23: Deviation between 3D-model-value and Matlab-value for the different nominal distances at 250mm.	50
Figure 4-24: Deviation between 3D-model-value and Matlab-value for the different nominal distances at 400mm.	51
Figure 4-25: Deviation between 3D-model-value and Matlab-value for the different nominal distances at 550mm.	51
Figure 4-26: Distances used in tilt estimation process. Adapted from (Muller P, 2012).	52
Figure 4-27: Ideal and real situation for tilt estimation process.	53
Figure 4-28: Distances used in slant estimation process. Adapted from (Muller P, 2012).	55
Figure 4-29: Ideal and real situation for slant estimation process.	56
Figure 4-30: Ideal and real situation for skew estimation process.	58
Figure 5-1: Linear relation between CMM and SPE.	62

List of Tables

Table 4-1: Input values for tilt estimation method	59
Table 4-2: Input values for slant estimation method	59
Table 4-3: Input values for skew estimation method	59
Table 5-1: Estimated tilt values	61
Table 5-2: Estimated slant values	61
Table 5-3: Estimation skew values	61

References

- Massimiliano Ferrucci, Richard K Leach, Claudiu Giusca, Simone Carmignato and Wim Dewulf (2015), 'Towards geometrical calibration of x-ray computed tomography systems—a review.'
- Muller P (2012), 'Coordinate metrology by traceable computed tomography' *PhD Thesis* Technical University of Denmark
- De Chiffre L., Carmignato S., Kruth J. P., Schmitt R., Weckenmann A. (2014), 'Industrial applications of computed tomography'. *CIRP Annals – Manufacturing Technology*, 63(2),
- Kruth J.P., Bartscher M., Carmignato S., Schmitt R., De Chiffre L., Weckenmann A. (2011), 'Computed tomography for dimensional metrology'
- Weckenmann A., Krämer P. (2010), 'Computed Tomography for Application in Manufacturing Metrology'. *Key Engineering Materials*, 437, pp. 73-78
- Bartscher M, Neuschaefer-Rube U, Wäldele F (2004), 'Computed Tomography— A Highly Potential Tool for Industrial Quality Control and Production Near Measurement'. *8th Intern. Symp. on Measurement and Quality Control in Production*.
- Pavel Müller (2011), 'Influence parameters in CT scanning' *DTU Mechanical Engineering Technical University of Denmark*
- Kak AC, Slaney M (1988), 'Principles of Computerized Tomographic Imaging'. *IEEE Press, New York*.
- L. De Chiffre, S. Carmignato, J.-P. Kruth, R. Schmitt, A. Weckenmann (2014) 'Industrial applications of computed tomography'
- M. Franz, Ch. Funk, J. Hiller, S. Kasperl, M. Krumm, S. Schröpfer (2009), 'Reliability of dimensional measurements by computed tomography for industrial applications'. *4th European-American Workshop on Reliability of NDE* 8 pp.
- R. A. Ketcham, W. D. Carlson (2001), 'Acquisition, optimization and interpretation of X-ray computed tomographic' *imagery: Applications to the geosciences, Computers & Geosciences* 27 pp. 381–400.
- T. Paul, Z. He (2008), 'Advanced NDT with high resolution computed tomography'. *Proceedings of the 17th World Conference on Nondestructive Testing (WCNDT)* 9 pp.
- S. Kasperl, J. Hiller, M. Krumm (2009), 'Computed tomography metrology in industrial research and development'. *MP Materials Testing* 51 (6) pp. 405–411
- U. Bonse, F. Busch (1996), 'X-ray computed microtomography (CT) using synchrotron radiation (SR)'. *Progress in Biophysics and Molecular Biology* 65 (1-2) pp. 133–169.
- O. Brunke, K. Brockdorf, S. Drews, B. Müller, T. Donath, J. Herzen, F. Beckmann (2008), 'Comparison between X-ray tube based and synchrotron radiation based CT'. *Proceedings of SPIE 7078* 12 pp.

- G. T. Herman (1979), 'Correction for beam hardening in computed tomography'. *Physics in Medicine and Biology* 21 (1) pp. 81–106.
- G. T. Herman (1980), 'Image Reconstruction from Projections: the Fundamentals of Computerized Tomography'. *2nd Edition, Academic Press, Inc, New York* ISBN 978-1-85233-617-2.
- R. A. Brooks, G. Di Chiro (1986), 'Beam hardening in X-ray reconstructive tomography'. *Physics in Medicine and Biology* 21 (3) pp. 390–398.
- S. Kasperl, J. Hiller (2009), 'Artefact correction at coordinate measuring with industrial X-ray computed tomography'. *Technisches Messen* 76 (9) pp. 401–409, doi:10.1524/teme.2009.09.18.
- Jochen Hiller, Peter Hornberger (1996), 'Measurement accuracy in X-ray computed tomography metrology' *Toward a systematic analysis of interference effects in tomographic imaging*
- Valentina Aloisi, Simone Carmignato, Joseph Schlecht, Eric Ferley (2017), 'Investigation on the effects of X-ray CT system geometrical misalignments on dimensional measurement errors'
- Kumar J, Attridge A, Wood P K C and Williams M A (2011), 'Analysis of the effect of cone-beam geometry and test object configuration on the measurement accuracy of a computed tomography scanner used for dimensional measurement' *Meas. Sci. Technol.* 22 035105
- Wenig P and Kasperl S (2006), 'Examination of the measurement uncertainty on dimensional measurements by x-ray computed tomography' *European Conf. on Non-Destructive Testing (Berlin, Germany)*
- Curry T S, Dowdey J E and Murr R E (1990), 'Christensen's physics of diagnostic radiology' 4th edition (Lea & Febiger)
- Hiller J, Maisl M and Reindl L M (2012), 'Physical characterization and performance evaluation of an X-ray micro-computed tomography system for dimensional metrology applications'. *Measurement Science and Technology* 23 085404
- Vogeler F, Verheecke W, Voet A and Kruth J (2011), 'Positional stability of 2D X-ray images for computer tomography'. *International Symposium of Digital Industrial Radiology and Computed Tomography (Proceedings) MO33*
- Reisinger S, Schmitt M and Volland V (2012), 'Geometric adjustment methods to improve reconstruction quality on rotational cone-beam systems' Website:
<http://www.ndt.net/article/ctc2012/papers/279.pdf> Accessed in March 2014
- Fröba T and Steffen J P (2011), 'Assessing the effect of focal spot movement on the accuracy of CT results by using a simulation technique' Website:
<http://www.ndt.net/article/ctc2012/papers/253.pdf> Accessed in March 2014

- Steffen J P and Fröba T (2011), 'Reducing the focal spot shift of microfocus X-ray tubes to increase the accuracy of CT-based dimensional measurement' Website:
<http://www.ndt.net/article/dir2011/papers/mo11ab~1.pdf> Accessed in March 2014
- Weiss D, Deffner A and Kuhn C (2010), 'Einfluß der Quellbewegung auf Reproduzierbarkeit und Antastabweichung im Röntgen-Computertomographen Website:
<http://www.ndt.net/article/ctc2010/papers/227.pdf> Accessed in March 2014
- Uhlman N , Salamon M, Burtzloff S, Porsch F, Johansson W, Nachtrab F and Hanke R (2008), 'Components and methods for highest resolution computed tomography' Website:
http://www.ndt.net/article/aero2008/aero08_M19_Uhlman_Norman.pdf Accessed in February 2014
- Fröba T and Steffen J (2011), 'The advancement of microfocus reflection tubes for industrial applications in measurement technology'. *50th Annual Conference of the British Institute of Non-Destructive Testing (Proceedings)*
- Nadia FLAY, Wenjuan SUN, Stephen BROWN, Richard LEACH, Thomas BLUMENSATH (2015), 'Investigation of the Focal Spot Drift in Industrial Cone-beam X-ray Computed Tomography'
- International Organization for Standardization (1998), 'Geometrical Product Specifications (GPS) – Inspection by measurement of workpieces and measuring equipment – Part 1: Decision rules for proving conformance or non-conformance with specifications'. *ISO 14253-1*.
- Trapet, E., Savio, E., De Chiffre, L. (2004), 'New advances in traceability of CMMs for almost the entire range of industrial dimensional metrology needs'. *CIRP Annals - Manufacturing Technology*, 53, 433–438.
- Nick Van Gestel (2011), 'Determining measurement uncertainties of feature measurements on CMMs'
- J.P. Kruth, P. Vanherck, and C. Van den Bergh (2001). 'Compensation of static and transient thermal errors on CMMs'. *CIRP Ann.*, 50(1):377–380.
- ISO/TS 15530-3 (2004). 'Geometrical Product Specifications (GPS) – Coordinate measuring machines (CMM): Technique for determining the uncertainty of measurement – Part 3: Use of calibrated workpieces or standards'.
- J.M. Baldwin, K.D. Summerhays, D.A. Campbell, and R.P. Henke (2004), 'Application of simulation software to coordinate measurement uncertainty evaluations'. *In Proceedings of the NCSL International Workshop and Symposium*.
- ISO 4288:1996 (1996). 'Geometrical Product Specifications (GPS) – Surface texture: Profile method – Rules and procedures for the assessment of surface texture.'
- Jintao Zhao, Xiaodong Hu, Jing Zou and Xiaotang Hu (2015), 'Geometric Parameters Estimation and Calibration in Cone-Beam Micro-CT'

S. Carmignato (2007), 'Traceability of dimensional measurements in computed tomography'. *In: Proceedings of 8th A.I.Te.M. Conference* 11 pp.

Müller, Pavel (2010), 'Use of reference objects for correction of measuring errors in X-ray computed tomography'.

H. Kunzmann, E. Trapet, F. Wäldele (1995), 'Results of the international comparison of ball plate measurements in CIRP and WECC'. *CIRP Annals – Manufacturing Technology* 44 (1) pp. 479–482, doi: [http://dx.doi.org/10.1016/S0007-8506\(07\)62367-1](http://dx.doi.org/10.1016/S0007-8506(07)62367-1).

H. N. Hansen, L. De Chiffre (1997), 'A combined optical and mechanical reference artefact for coordinate measuring machines'. *CIRP Annals – Manufacturing Technology* 46 (1) pp. 467–470, [http://dx.doi.org/10.1016/S0007-8506\(07\)60867-1](http://dx.doi.org/10.1016/S0007-8506(07)60867-1).

L. De Chiffre, H. N. Hansen, R. E. Morace (2005), 'Comparison of coordinate measuring machines using an optomechanical hole plate'. *CIRP Annals - Manufacturing Technology* 54 (1) pp. 479–482, [http://dx.doi.org/10.1016/S0007-8506\(07\)60149-8](http://dx.doi.org/10.1016/S0007-8506(07)60149-8).

Appendix

In the appendix folder of the thesis, there are: an Excel document with all plots and data of measurements from CT and CMM and the Matlab code used for detecting the spheres.

